PHYSICAL REVIEW A **104**, 053703 (2021)

Waveguide-QED platform for synthetic quantum matter

Ying Dong,[1,2] J. Taylor,[2,3] Youn Seok Lee,[2] H. R. Kong,[2,3] and K. S. Choi[2,3,*]
[1]*Research Center for Quantum Sensing, Zhejiang Lab, Hangzhou 311121, China*
[2]*Institute for Quantum Computing and Department of Physics and Astronomy, University of Waterloo, Waterloo, Ontario, Canada N2L 3G1*
[3]*Q-Block Computing Inc., Kitchener, Ontario, Canada N2C 2C8*

(Received 10 June 2021; revised 20 September 2021; accepted 27 September 2021; published 8 November 2021)

An exciting frontier in quantum information science is the realization and control of complex quantum many-body systems. The hybrid nanophotonic system with cold atoms has emerged as a paradigmatic platform for realizing long-range spin models from the bottom up, exploiting their modal geometry and group dispersion for tailored interactions. An important challenge is the physical limitation imposed by the photonic bath, constraining the types of local Hamiltonians that decompose the available physical models and restricting the spatial dimensions to that of the dielectric media. However, at the nanoscopic scale, atom-field interaction inherently accompanies significant driven-dissipative quantum forces that may be tamed as a new form of a mediator for controlling the atomic internal states. Here we formulate a quantum optics toolbox for constructing universal quantum matter with individual atoms in the vicinity of one-dimensional photonic crystal waveguides. The enabling platform synthesizes analog quantum materials of universal 2-local Hamiltonian graphs mediated by phononic superfluids of the trapped atoms. We generalize our microscopic theory of an analog universal quantum simulator to the development of dynamical gauge fields. In the spirit of gauge theories, we investigate emergent lattice models of arbitrary graphs, for which strongly coupled SU(n) excitations are driven by an underlying multibody interaction. As a minimal model in the infrared, we explore the realization of an archetypical strong-coupling quantum field theory, the SU(n) Wess-Zumino-Witten model, and discuss a diagnostic tool to map the conformal data of the field theory to the static and dynamical correlators of the fluctuating photons in the guided mode.

DOI: 10.1103/PhysRevA.104.053703

I. INTRODUCTION

One of the central problems in quantum information science and condensed matter physics is to create and control strongly interacting quantum systems and to measure the equilibrium and nonequilibrium properties of the many-body system [1–3]. Recent experiments with ultracold atoms have extended the ranges of unconventional phenomena that may be accessed. A common thread in these efforts is the quest to design the Hamiltonian by harnessing the natural interactions available between cold atoms [4]. Much of the focus has largely been on analog and Floquet quantum systems. However, these approaches are limited in their applicability to complex target Hamiltonians whose description departs significantly from the microscopic model of the simulator.

A parallel development has been the exploration of computational complexity of local Hamiltonians, whose ground-state properties cannot be efficiently obtained even by a digital quantum computer. An example of such a quantum-Merlin-Arthur (QMA) problem is to find the ground state of 2-local Hamiltonians $\hat{H}_{\text{QMA}} = \sum_{ij} \hat{h}_{ij}$, where the local decomposition $\hat{h}_{ij}$ consists of at most two-body SU(2) operators. More generally, arbitrarily complex quantum matter $\hat{H}_{\text{target}}$ can be emulated with a seemingly simpler but QMA-complete lattice model $\hat{H}_{\text{QMA}}$ [5], in that all physical properties and local structures of $\hat{H}_{\text{target}}$ can be efficiently mapped onto the universal model $\hat{H}_{\text{QMA}}$. Likewise, a quantum simulator that realizes analog Hamiltonians $\hat{H}_{\text{QMA}}$ can be adapted for universal quantum computation in the spirits of cellular automata and Hamiltonian computation [6–8].

With recent developments in atom-photon interfaces with photonic crystals [9–19], there has been significant interest in assembling quantum many-body systems by garnering the control over individual quantum systems [1–4]. With the atomic transition frequency residing within the photonic band gap (PBG), the underlying lattice of atoms cannot dissipate propagating waves into the guided modes (GMs) of the photonic structure. However, the mere presence of the atoms at sites i, j in a waveguide seeds dynamic defect modes that support stable atom-field bound states in the form of evanescent waves [9,10,20–22], mediating exchange interaction $J_{|i-j|}\vec{\hat{\sigma}}^{(i)} \cdot \vec{\hat{\sigma}}^{(j)}$ between the trapped atoms [23,24]. With auxiliary Raman sidebands and digital time steps [1], the phase-amplitude function $J_{|i-j|}$ can be engineered for atoms coupled to one-dimensional (1D) and 2D photonic crystal waveguides (PCWs) and realize translationally invariant pairwise models for quantum magnetism, constrained by the dimension of the dielectric [25]. Conversely, photons propagating through the guided mode exhibit novel quantum transport and many-body phenomena [26–30].

---

[*] kyung.choi@uwaterloo.ca

At the nanoscale, the atom-field interaction is modified by the electromagnetic vacuum of the dielectric, consisting of both the passive photonic structure and the active emitters. Such a quantum dielectric is inherently renormalized by the strong coherent and dissipative radiative forces between the atoms. Indeed, complex spin-mechanical textures arise through localized spin-dependent photon-mediated forces [31]. More generally, nanoscopic quantum forces modify the mechanical vacuum of the atomic motion, where Bogoliubov phonons are distributed across the atomic sample as a collective bath that in turn couples to the spin system. The dissipative nature of these forces in PCWs may be exploited to stabilize and self-organize new forms of mechanical phases of quantum matter, and complex observables may be constructed for the detection of highly entangled quantum systems.

Here we harness the coherent coupling between atomic motion and internal states in 1D PCWs for the realization of analog universal quantum matter. We develop a low-energy theory for the quantum motion of the trapped atoms in the band-gap regime of waveguide QED. By coupling Bogoliubov phonons to the spin matter, we realize a fully programmable lattice spin system $\hat{\rho}_s$ for neutral atoms. In our approach, an arbitrary binary interaction $\hat{h}_{ij} \simeq \sum_{\alpha,\beta} J^{(i,j)}_{\alpha\beta} \hat{\sigma}^{(i)}_{\alpha} \hat{\sigma}^{(j)}_{\beta}$ is realized for any combination of SU(2)-spin operators $\hat{\sigma}^{(i)}_{\alpha}, \hat{\sigma}^{(j)}_{\beta}$ with $\alpha, \beta \in \{0, x, y, z\}$ between sites i and j. Our spin network $\hat{\rho}_s$ is described by Hamiltonian graphs with connectivity i, j that can no longer be represented by spatial lattices and dimensions and realizes the universal 2-local quantum matter $\hat{H}_{\text{QMA}} = \sum_{i,j} \hat{h}_{ij}$ in a fully analog manner. Our waveguide QED simulator, stabilizing $\hat{H}_{\text{QMA}}$, is universal, in that any k-local Hamiltonian $\hat{H}_{\text{target}}$ of arbitrary connectivity can be embedded into the low-energy sector of $\hat{H}_{\text{QMA}}$ [5]. This notion of universality is strong in that any physical phenomena of $\hat{H}_{\text{target}}$ must correspond to an emergent behavior of the analog simulator $\hat{H}_{\text{QMA}}$ in the long-distance limit.

Moreover, we formulate a hardware-efficient protocol to design dynamical gauge structures of many-body system and realize a plethora of SU(n) models with our waveguide QED simulator. Motivated by gauge fixing in quantum spin glasses and color codes, we describe a general construction for which the low-energy physics of $\hat{\rho}_s$ encompasses the full scope of binary lattice models for SU(n)-spin excitations with local constraints that protect the many-body wave function $\hat{\rho}_s$ from errors. Here atomic arrays constrained by their local symmetries are encoded into logical SU(n) blocks, and dynamical U(1)-gauge fields mediate programmable long-range interactions between the logical blocks.

Utilizing these capabilities, we demonstrate the versatility of our universal analog simulator by constructing chiral-spin liquids [32] and holographic strange metals [33,34]. As a primordial example to the tower of phases, we explore the physics of SU(3) Wess-Zumino-Witten conformal field theory (CFT), a holographic dual to Chern-Simons gravity [35], by encoding the target CFT onto the low-energy sector of our waveguide QED simulator. We investigate the critical scaling of CFT entanglement and the dynamics of semionic quasiparticle excitations, as reflected by the fluctuating photons of the PCW. Our networked approach provides powerful tools for controlling analog quantum systems with complexities far beyond the regular spin lattices heretofore explored.

TABLE I. Final design variables for the SPCW with slab index $n = 2$. The uncertainty ±1 nm is added for the normal distributions of the disordered SPCW structure in Fig. 7.

Structural parameter	Value
Lattice constant a_0	366 ± 1 nm
Slot width w	226 ± 1 nm
Slab thickness t	200 ± 1 nm
Squircle radius r_s	99 ± 1 nm
Secondary radius r'	105 ± 1 nm
Hole radius r	109 ± 1 nm
First line shift l	413 ± 1 nm
Secondary line shift m	729 ± 1 nm
Squircle height a	79 ± 1 nm
Squircle width b	124 ± 1 nm

The structure of this paper is organized as follows. In Sec. II we investigate the interplay among waveguide photons, atomic external motion, and internal energy levels and establish the low-energy theory for an analog quantum simulator of universal Hamiltonians [5]. In Sec. III we discuss the realization of a chiral-spin liquid on kagome lattice and the detailed design of Raman sidebands. In Sec. IV we introduce the realization of SU(n)-spin models by gauging N two-level atoms to a constrained subspace. With this logical encoding, we construct a general SU(n) Hamiltonian for the waveguide QED platform. In Sec. V we analyze the emergence of a minimal SU(3) Wess-Zumino-Witten model with matrix-product states and discuss operational metrics for its diagnosis. In Sec. VI we discuss the experimental feasibility and summarize the advances made in this work.

II. PLATFORM

A. Lamb shifts in PCWs: Phononic Hubbard model

Our approach is based upon the unique capability of PCWs to induce strong photon-mediated forces between proximal neutral atoms and to create many-body states of internal spin and external motion. By engineering the QED vacuum of the PCW, we synthesize coherent mechanical coupling between the trapped atoms and renormalize the atomic array into a mechanical quantum network. Long-range interaction of the universal Hamiltonian $\hat{H}_{\text{QMA}} = \sum_{i,j} \hat{h}_{i,j}$ is mediated through the phononic quantum channels with full control over the decompositions $\hat{h}_{i,j}$ and their connectivity i, j.

As shown in Fig. 1, our basic building block is a 1D lattice of neutral atoms at positions x_i strongly coupled to a dispersive PCW with mode function $u_{k_0}(x)$ represented by the red line of Fig. 1(b). The band edge at frequency w_b is red detuned by $\Delta_b = \omega - \omega_b > 0$, so the atomic transition frequency ω lies within the band gap. Each atom is tightly localized at the antinodes of $u_{k_0}(x)$ with trap frequency ω_t and lattice constant a_0 by a nanoscopic optical potential $V_T = V_0 \sin^2 k_0 x$ with a trapping field at a higher-order GM (blue line). In Appendix B we analyze a versatile candidate structure (silicon nitride squircle PCW) with highly tunable GMs in terms of

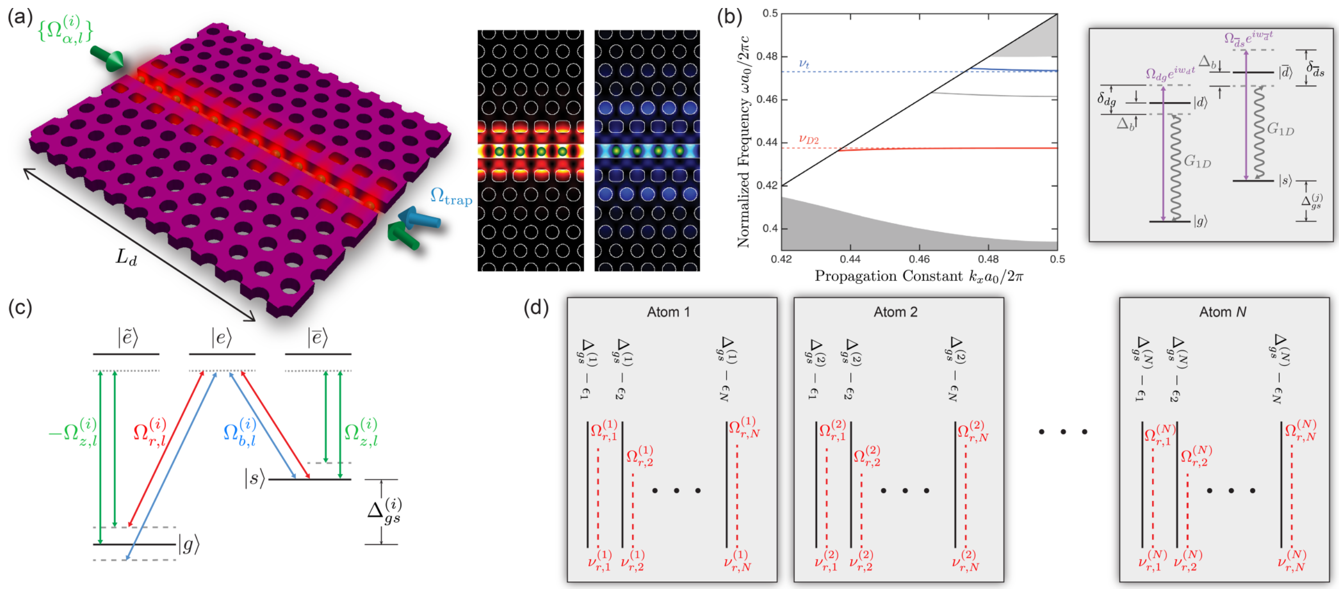

FIG. 1. Complex quantum many-body physics with waveguide QED systems. (a) Exemplary waveguide QED spin network. The slotted squircle photonic crystal waveguide (SPCW) enables a versatile platform for highly tunable defect guided modes, with the supermodes shown in the inset. As a candidate PCW, the structural parameters are provided in Table I and discussed in Appendix B. Green spheres represent the trapped atoms. The inset shows a contour map of the intensity profile for TE supermodes for exciting (trapping) Cs atoms at wavelengths $\lambda_p = 852$ nm ($\lambda_t = 794$ nm). (b) Normalized band diagram for the supermodes of the SPCW. The inset shows two lasers $\Omega_{dg}, \Omega_{\bar d s}$ with detunings $\delta_{dg}, \delta_{\bar d s}$ that create strong photonic Lamb shifts $\sim e^{-|i-j|a_0/L_c}$ between two atoms localized within a photonic band gap [20]. The band gap is detuned by Δ_b with respect to the transition frequency. (c) Raman couplings synthesize programmable interactions between two atoms at sites $i, j \in \{1, \dots, N\}$ for any combination of SU(2) spin operators. Site-resolved addressing with spatially global fields $\Omega^{(i)}_{\alpha,l}$ (in the frequency domain) is achieved through inhomogeneous Zeeman shifts $\Delta^{(i)}_{gs}$ through intermediated excited states $|\tilde e\rangle, |e\rangle, |\bar e\rangle$ with $\alpha \in \{r, b, z\}$. (d) Raman engineering. Programmable Raman fields $\Omega^{(i)}_{\alpha,l}$ selectively couple internal states $|g\rangle, |s\rangle$ of atom i to the Bogoliubov phononic mode $l \in \{1, \dots, N\}$ with two-photon detuning $\nu^{(i)}_l$. Each single sideband mode with frequency $\nu^{(i)}_l$ (red dashed line) is nearly resonant to $\Delta^{(i)}_{gs} - \epsilon_l$ (black solid line), where ϵ_l is the phonon spectrum. Only the red sideband couplings are depicted for simplicity.

the TE photonic band gap, effective photon mass m_e, and mode area $A_{\rm eff}$ near the band edge $k_x = k_0$ [see Fig. 1(b) for the band diagram]. Here $|g\rangle$ and $|s\rangle$ are the two hyperfine ground states that define the computational basis $\mathcal{C}$ of the waveguide QED simulator, and the ground states respectively couple to excited states $|d\rangle$ and $|\bar d\rangle$, which will be eliminated to induce a pure mechanical coupling between the atoms.

The atom-PCW Hamiltonian reads $\hat H_{\rm PCW} = \int d\boldsymbol{x} \int_0^\infty d\omega\, \hat{\boldsymbol{f}}^\dagger(\boldsymbol{x}, \omega)\hat{\boldsymbol{f}}(\boldsymbol{x}, \omega) + \sum_i(\omega_d \sigma^{(i)}_{dd} + \omega_{\bar d}\sigma^{(i)}_{\bar d\bar d} + \Delta_{gs}\, \sigma^{(i)}_{ss}) + \sum_{i=1}^{N_a}\sum_{\mu=dg,\bar d s}[\int_0^\infty d\omega \boldsymbol{E}(\boldsymbol{x}_i, \omega)\cdot \boldsymbol{d}_\mu \hat\sigma^{(i)}_\mu + \Omega_\mu \sigma^{(i)}_\mu\, e^{-i\nu_\mu t}]$, where $\boldsymbol{d}_{dg(\bar d s)}$ is the transition dipole momentum from $|g(s)\rangle$ to $|d(\bar d)\rangle$ and $\Omega_{dg(\bar d s)}$ is the Rabi frequency of the pumping fields with frequency $\nu_{dg(\bar d s)}$ that couples $|g(s)\rangle$ and $|d(\bar d)\rangle$. We assume $\boldsymbol{d}_{dg} = \boldsymbol{d}_{\bar d s} = \boldsymbol{d}$. The electric field in the PCW can be represented by classical Green's function $\boldsymbol{G}(\boldsymbol{x}, \boldsymbol{x}', \omega)$ as $\hat{\boldsymbol{E}}(\boldsymbol{x}, \omega) = i\mu_0\omega^2\sqrt{\frac{\epsilon_0}{\pi}} \int d\boldsymbol{x}' \sqrt{{\rm Im}\{\epsilon(\boldsymbol{x}', \omega)\}}\boldsymbol{G}(\boldsymbol{x}, \boldsymbol{x}', \omega)\hat{\boldsymbol{f}}(\boldsymbol{x}, \omega)$, where $\hat{\boldsymbol{f}}(\boldsymbol{x}, \omega)$ represents the quantized excitation of the dielectric with permittivity $\epsilon(\boldsymbol{x}', \omega)$ [36,37].

In the limit $f_{dg(\bar d s)} = \Omega_{dg(\bar d s)}/\delta_{dg(\bar d s)} = f \ll 1$ where $\delta_{dg(\bar d s)} = \nu_{dg(\bar d s)} - \omega_{d(\bar d)}$, we adiabatically eliminate the excited states $|d\rangle$ and $|\bar d\rangle$ from the system and integrate out the photonic modes [38–41]. We thereby obtain the low-energy Liouvillian dynamics $\dot{\hat\rho} = -i[\hat H^{\rm int}_M, \hat\rho] + \mathcal{L}_0[\hat\rho] + \mathcal{L}_M[\hat\rho]$ with a purely mechanical Hamiltonian

$$\hat H^{\rm int}_M = f^2 \Delta_{\rm Lamb}(\hat{\boldsymbol{x}}_i, \hat{\boldsymbol{x}}_j)\hat\sigma^{(i)}_0\hat\sigma^{(j)}_0 \tag{1}$$

and the respective Lindblad superoperators $\mathcal{L}_0[\hat\rho] = \sum_{i,j}\frac{\Gamma_{ij}f^2}{2}(2\hat\sigma^{(i)}_0\hat\rho\hat\sigma^{(j)}_0 - \hat\sigma^{(i)}_0\hat\sigma^{(j)}_0\hat\rho - \hat\rho\hat\sigma^{(i)}_0\hat\sigma^{(j)}_0)$ and $\mathcal{L}_M[\hat\rho] = \sum_{i,j}\frac{\Gamma_{ij}f^2}{2}(2e^{ik\hat{\boldsymbol{x}}_i}\hat\rho e^{-ik\hat{\boldsymbol{x}}_j} - e^{ik(\hat{\boldsymbol{x}}_i-\hat{\boldsymbol{x}}_j)}\hat\rho - \hat\rho e^{ik(\hat{\boldsymbol{x}}_j-\hat{\boldsymbol{x}}_i)})$ acting on the internal and external degrees of freedom (DOF), where $\hat\sigma_0 = |g\rangle\langle g| + |s\rangle\langle s|$ is the identity spin operator in $\mathcal{C}$. The photonic Lamb shift and correlated dissipation, modified by the PCW, are given by

$$\Delta_{\rm Lamb}(\hat{\boldsymbol{x}}_i, \hat{\boldsymbol{x}}_j) = 2\mu_0\omega_b^2 \boldsymbol{d}^* \cdot {\rm Re}[\boldsymbol{G}_s(\hat{\boldsymbol{x}}_i, \hat{\boldsymbol{x}}_j, \omega_b)]\cdot \boldsymbol{d}, \tag{2}$$

$$\Gamma_{ij}(\hat{\boldsymbol{x}}_i, \hat{\boldsymbol{x}}_j) = \mu_0\omega_b^2 \boldsymbol{d}^* \cdot {\rm Im}[\boldsymbol{G}(\hat{\boldsymbol{x}}_i, \hat{\boldsymbol{x}}_j, \omega_b)]\cdot \boldsymbol{d}, \tag{3}$$

respectively, where $\boldsymbol{G}_s = \boldsymbol{G} - \boldsymbol{G}_0$ is the scattering Green's function relative to the vacuum term $\boldsymbol{G}_0$ (see Appendix B). Importantly, the coherent dynamics of Eq. (1) is decoupled from the internal states within the computational space $\mathcal{C}$ and only induces a nonlocal mechanical interaction between the trapped atoms. The state independence of Eq. (1) is crucial, as the photon-mediated spin-exchange coupling cannot break the translational invariance intrinsic to the photonic crystal structure [20]. Instead, our quantum simulator emerges from the programmable interactions between the internal states and the Bogoliubov modes of Eq. (1). Indeed, seen from the atoms, the correlated radiative decay Γ_{ij} does not directly contribute to the dynamics of computational subspace $\mathcal{C}$ but induces mechanical damping to the atomic quantum motion.

In our case, the GM near the band edge $k_x = k_0$ (corresponding frequency ω_b) exhibits an extremely flat band $w_k - w_b \simeq -\frac{1}{2m_e}(k_x - k_0)^2$ and the GM photons acquire large mass $1/m_e = -(\partial^2 w_k/\partial k_x^2)$ [see Fig. 1(b) for the first Brillouin zone]. In the reactive regime of the PBG, the atoms predominantly couple to this band edge and the Green's function is approximated by

$$G_{\mathrm{1D}}(\hat{x}_i, \hat{x}_j) = J_{\mathrm{1D}} u_{k_0}(x_i) u_{k_0}(x_j) e^{-|\hat{x}_i - \hat{x}_j|/L_c}, \tag{4}$$

where the localization length $L_c = \sqrt{1/2m_e\Delta_e} \sim a_0$ is controlled by the detuning $\Delta_e \simeq 2\Delta_b$ of the pumping field from band edge. Here $J_{\mathrm{1D}} = -\frac{c^2}{2\omega_b L_c A_{\mathrm{eff}}} \frac{1}{\Delta_e + i\kappa/2}$ is the coupling rate to the PCW with effective mode area $A_{\mathrm{eff}} \simeq \lambda^2$, mode function $u_{k_0}(x_i)$ at the band edge, and decay rate κ (κ_0) in the band gap (at the band edge). The correlated Lamb shift thereby provides the tunneling interaction $\hat{H}_M = f^2 \Delta_{\mathrm{1D}} e^{-|\hat{x}_i - \hat{x}_j|/L_c}$ between local phonons pinned on the lattice sites x_i and x_j, with $\Delta_{\mathrm{1D}} = \frac{\omega_b d^2 \Delta_e}{\epsilon_0 L_c A_{\mathrm{eff}}(\Delta_e^2 + \kappa^2/4)}$. Importantly, the collective damping $\Gamma_{\mathrm{1D}} \sim \tilde{\Gamma}_{\mathrm{1D}} \exp(-L_d/L_c)$ is exponentially inhibited for a finite device length L_d, with $\tilde{\Gamma}_{\mathrm{1D}} = \frac{\omega_b d^2 \kappa_0}{2\epsilon_0 L_c A_{\mathrm{eff}}(\Delta_e^2 + \kappa_0^2/4)}$, and the figure of merit $\mathcal{F} = \Delta_{\mathrm{1D}}/\Gamma_{\mathrm{1D}} \sim \exp(L_d/L_c) \gg 1$ is favorable for massive photons with flat bands and long device length $L_d \gg L_c$.

To make progress analytically, we consider the case of $L_c \sim a_0$ with massive photons (flat bands in the PCW), where the atom-atom interaction reduces to nearest-neighboring terms. We thereby expand the mechanical Hamiltonian $\hat{H}_M$ around the equilibrium positions to the second order of the zero-point motion $x_0 = \sqrt{\hbar/2m\omega_t}$ and obtain the quadratic form

$$H_M = \sum_i \frac{\hat{p}_i^2}{2m} + \frac{m\omega_t^2}{2}\hat{x}_i^2 - \frac{\hbar g_m}{L_c^2}\hat{x}_i\hat{x}_{i+1} + O\big(\hat{x}_i^4\big) \tag{5}$$

for the mechanical coupling constant $g_m = f^2 \Delta_{\mathrm{Lamb}}$ and the trap frequency ω_t. With a first-type sine transform $B_{jk} = \frac{1}{\sqrt{N}} \sin(i\frac{\pi}{N+1}jk)$, we diagonalize $H_M = \sum_{l=1}^{N} \epsilon_l \hat{\beta}_l^\dagger \hat{\beta}_l$, whose quasiparticles are the Bogoliubov phonons $\{\hat{\beta}_l\}$ with spectrum $\epsilon_l = \sqrt{\omega_t^2 + \frac{2\hbar g_m x_0^2}{L_c^2}\cos(\frac{\pi}{N+1}l)}$ with momentum-space mode indices l. For nanoscopic optical potentials with $k_x x_0 \lll 1$, Eq. (5) describes a 1D Bose-Hubbard model for atomic motion with on-site (long-range) interaction $\sim\hat{x}_i^4/x_0^4$ ($|\hat{x}_i - \hat{x}_j|^4/L_c^4$), where the Bogoliubov phonons are excited out of the superfluid vacuum. The radiative damping Γ_{1D} gives rise to motional decoherence $\mathcal{L}_M[\hat{\rho}_{MA}] = \sum_l \frac{\gamma_m}{2}(2\hat{\hat{x}}_l \hat{\rho}_{MA} \hat{\hat{x}}_l - \{\hat{\hat{x}}_l^2, \hat{\rho}_{MA}\})$ with damping $\gamma_m = \frac{g_m x_0^2}{\Delta_e L_c^2} \kappa e^{-L_d/L_c}$ and quadrature $\hat{\hat{x}}_l = \hat{\beta}_l + \hat{\beta}_l^\dagger$. We note that the requirement for $L_c \sim a_0$ is not intrinsic to the protocol, as the long-range interaction $L_c > a_0$ only modifies the frequencies of the phononic bands. The momentum-space Bogoliubov modes constitute the frequency-selective channels of an all-to-all connected mechanical quantum network and coherently mediate the interactions between the atomic nodes, transforming the atomic array into a universal quantum matter.

B. Networked universal quantum matter

To mediate the universal lattice model via the phononic channels, we gain independent control over the interaction coefficients between any atom pair i, j by way of Raman engineering in the sideband-resolved limit. This is ensured in the reactive regime of PCWs, because the mechanical damping constant γ_m is exponentially suppressed by $\mathcal{F} \sim \exp(L_d/L_c) \gg 1$ relative to the phonon spread. As shown in Fig. 1(c), we distinguish the coupling of an individual atom i to a particular Bogoliubov mode l with the site-dependent ground-state energy shift $\hat{H}_A = \sum_i \Delta_{gs}^{(i)} \hat{\sigma}_z^{(i)}$, with $\Delta_{gs}^{(i)} = \Delta_{gs} + g_F m_F B(x_i)$ in the form of a linear Zeeman gradient $B(x_i)$ [25]. The ground-state shift $\delta\Delta_{gs}$ between neighboring sites is larger than the width of the phonon spectrum $|\epsilon_N - \epsilon_1|$, so the frequency difference $\Delta_{gs}^{(i)} - \epsilon_l$ is different for all pairs of (i, l) [see Fig. 1(d)].

Then we introduce the spatially global Raman interaction $\hat{H} = \hat{H}_M + \hat{H}_A + \sum_{i,j} \sum_{\alpha,l} \frac{\Omega_{\alpha,l}^{(j)}}{2} \hat{\sigma}_\alpha^{(i)} \sin(k_{\alpha,l}^{(j)} \hat{x}_i) e^{-i\nu_{\alpha,l}^{(j)} t} + \mathrm{H.c.}$ [42–45] with N^2 frequency sidebands to the atom chain through the GM, where $k_{\alpha,l}^{(i)} \simeq k$ and $\nu_{\alpha,l}^{(i)}$ denote the wave number and frequency for the Raman fields that couple the spin operator $\hat{\sigma}_\alpha^{(i)}$ of atom i with $\alpha \in \{\pm, z\}$ to the Bogoliubov mode l with $\alpha \in \{\pm, z\}$. By expanding $\sin(k\hat{x}_i) \simeq \sum_l \eta_0 B_{il}(\hat{\beta}_l^\dagger + \hat{\beta}_l)$ in the Lamb-Dicke limit with $\eta_0 = x_0/a_0$ and switching to the interaction picture, we find $\hat{H}_{MA} = \sum_{\alpha,i,j,l} \Omega_{\alpha,l}^{(j)} \hat{\sigma}_\alpha^{(i)} e^{-i(\nu_{\alpha,l}^{(j)} - \zeta_\alpha \Delta_{gs}^{(i)})t} \eta_0 B_{il} \hat{\beta}_l^\dagger e^{i\epsilon_l t} + \mathrm{H.c.}$, with $\zeta_\alpha = \pm 1, 0$ for $\alpha = \pm, z$. As $\Delta_{\alpha,l}^{(i)} = \nu_{\alpha,l}^{(i)} - \zeta_\alpha \Delta_{gs}^{(i)} + \epsilon_l \ll |\epsilon_l - \epsilon_{l-1}| \ll \delta\Delta_{gs}$, we integrate over the rapidly oscillating terms and leave only the slowly varying terms $\sim \exp[i(\nu_{\alpha,l}^{(i)} - \zeta_\alpha \omega_A^{(i)} + \omega_l)t]$ and obtain the spin-mechanical Hamiltonian $\hat{H}_{MA} = \sum_{i,l} \sum_{\alpha \in \{x,y,z\}} \frac{\eta_0 \Omega_{\alpha,l}^{(i)}}{2} B_{il} \hat{\sigma}_\alpha^{(i)} \hat{\beta}_l e^{-i\Delta_l t} + \mathrm{H.c.}$, thereby coupling the spin operator $\hat{\sigma}_\alpha^{(i)}$ at site x_i to a particular Bogoliubov mode l. Here the detuning $\Delta_{\alpha,l}^{(i)} = \Delta_M$ is chosen to be identical for all phononic modes l, atoms i, and spin operator types α and the Rabi frequencies are transformed as $\Omega_{x,l}^{(i)} = (\Omega_{+,l}^{(i)} + \Omega_{-,l}^{(i)})/2$ and $\Omega_{y,l}^{(i)} = i(\Omega_{+,l}^{(i)} - \Omega_{-,l}^{(i)})/2$.

By projecting the master equation to the computational subspace $\mathcal{C}$ [46], we obtain the open-system dynamics $\dot{\hat{\rho}}_A = -i[\hat{H}_{\mathrm{QMA}}, \hat{\rho}_A] + \sum_\alpha \mathcal{L}[\hat{\rho}_A]$ for the spin system, governed by the universal Hamiltonian

$$\hat{H}_{\mathrm{QMA}} \simeq \sum_{i,j,\alpha,\beta} J_{\alpha,\beta}^{(i,j)} \hat{\sigma}_\alpha^{(i)} \hat{\sigma}_\beta^{(j)} + \sum_{i,\gamma} h_\gamma^{(i)} \hat{\sigma}_\gamma^{(i)} \tag{6}$$

and the correlated dissipation

$$\mathcal{L}[\hat{\rho}_A] = \sum_{i,j,\alpha,\beta} \frac{\gamma_{\alpha,\beta}^{(i,j)}}{2} \big(2\hat{\sigma}_\beta^{(i)} \hat{\rho}_A \hat{\sigma}_\alpha^{(j)} - \big\{\hat{\sigma}_\alpha^{(i)} \hat{\sigma}_\beta^{(j)}, \hat{\rho}_A\big\}\big) \tag{7}$$

for any combination of $\alpha, \beta, \gamma \in \{x, y, z\}$ and between any two spins at sites i, j. Importantly, the exchange interaction $J_{\alpha,\beta}^{(i,j)}$ and the bias field $h_\gamma^{(i)}$ can be arbitrarily designed by solving a set of nonlinear equations $J_{\alpha,\beta}^{(i,j)} = 2\,\mathrm{Re}[\sum_l \tilde{\Omega}_{\alpha,l}^{(i)} \tilde{\Omega}_{\beta,l}^{(j)*}/\Delta_M]$ and $h_\gamma^{(i)} = -2\epsilon_{\alpha\beta\gamma} \mathrm{Im}[\sum_l \tilde{\Omega}_{\alpha,l}^{(i)} \tilde{\Omega}_{\beta,l}^{(i)*}/\Delta_M]$, where $\tilde{\Omega}_{\alpha,l}^{(i)} = \eta_0 \Omega_{\alpha,l}^{(i)} B_{il}$ and Levi-Cività symbol $\epsilon_{\alpha\beta\gamma}$. Namely, we have $6N^2$ DOFs for the sidebands $\{\Omega_{\alpha,l}^{(i)}\}$ from the nonlinear equations, while only $3(3N^2 - N)/2$ independent parameters $\{J_{\alpha,\beta}^{(i,j)}, h_{\gamma}^{(i)}\}$ are required to represent the universal model $\hat{H}_{\mathrm{QMA}}$. Hence, for any set $\{J_{\alpha,\beta}^{(i,j)}, h_{\gamma}^{(i)}\}$, at least one solution $\{\Omega_{\alpha,l}^{(i)}, \Delta_M\}$ can be obtained for the target model within certain physical constraints (e.g., laser power). We envisage that the Raman sideband matrices $\{\Omega_{\alpha,l}^{(i)}\}$ are real-time tunable. The Hamiltonian $\hat{H}_{\mathrm{QMA}}(t)$ can be evolved to map out complex phase diagrams of many-body models and be globally quenched to study out-of-equilibrium dynamics. The frequency sidebands $\{\Omega_{\alpha,l}^{(i)}\}$ can be streamed by the time-domain response function $\Omega(t)$ using a single-mode phase-amplitude modulator. The dissipation rate is evaluated as $\gamma_{\alpha,\beta}^{(i,j)} = \frac{\gamma_m}{\Delta_M} J_{\alpha,\beta}^{(i,j)} + \gamma_A \delta_{i,j}$, where δ_{ij} denotes the Kronecker symbol. The coherence-to-dissipation ratio $C = J_{\alpha\beta}/\gamma_{\alpha\beta} = \mathcal{F}/N \sim \exp(L_d/L_c)/N \gg 1$ of our simulator improves exponentially in the reactive regime. In practice, C is constrained by γ_A due to the finite $\Omega_{\alpha,l}$ and Δ_M of the Raman fields.

III. CHIRAL-SPIN LIQUIDS IN A KAGOME LATTICE

Frustration in lattice spin systems, in which local energy constraints cannot all be satisfied, can lead to deconfined phases of quantum spin liquids (QSLs). In a QSL, quantum fluctuations drive the collective state of the spins into highly entangled quantum matter, such as the resonating valence bond state in Z_2-spin liquids, whose emergent topological properties can only be described in terms of long-range entanglement [32]. Unlike gapped Z_2-spin liquids, chiral-spin liquids (CSLs) spontaneously break the time-reversal and parity symmetry, while preserving other symmetries, and host fractional quasiparticle excitations with topological order [47]. Such a CSL is thought to be a parent state of the illusive anyonic superconductor.

As an example of Eq. (6), we discuss a method of creating the topological CSL discovered by Kalmeyer and Laughlin, a bosonic analog of the celebrated fractional quantum Hall effect [48–50], with our waveguide QED toolboxes. We consider an anisotropic antiferromagnetic XXZ Hamiltonian

$$\hat{H}_{\mathrm{CSL}} = \sum_{\langle ij\rangle} \left(J_{\perp}\hat{\sigma}_{\perp}^{(i)}\hat{\sigma}_{\perp}^{(j)} + J_{ZZ}\hat{\sigma}_{z}^{(i)}\hat{\sigma}_{z}^{(j)}\right) + \lambda\hat{\chi} \tag{8}$$

on a kagome lattice with tunable spin chirality $\hat{\chi}$. Despite the physical dimension of the atomic lattice in 1D PCWs, our toolboxes allow the spins to sit on a synthetic geometry provided by the connectivity of the translationally variant spin-exchange couplings, as depicted by the 2D kagome lattice in Fig. 2. With $\lambda = 0$, $\hat{H}_{\mathrm{CSL}}$ reduces to the kagome XXZ antiferromagnet, which has been widely studied for its time-reversal symmetric Z_2-spin liquid [51,52].

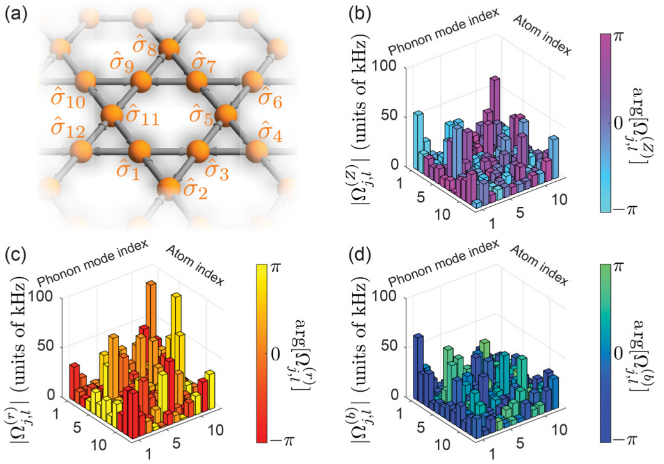

FIG. 2. Chiral-spin liquid phase in a kagome lattice with vector-spin coupling. (a) Antiferromagnetic Heisenberg model $\hat{H}_{\mathrm{AF}}$ with Dzyaloshinskii-Moriya interaction $\hat{\chi}_{\mathrm{vector}}$ illustrated for spins in an artificial kagome lattice. The gray arrows indicate the sign of the vector coupling in $\hat{\chi}_{\mathrm{vector}}$. (b)–(d) Raman sidebands realize $\hat{H}_{\mathrm{CSL}}$ in Eq. (8) with tunable chirality $\hat{\chi}_{\mathrm{vector}}$ for $J_{\perp} = J_{ZZ} = 0.5$ kHz and $\lambda = 0.1$ kHz. Adiabatic evolution through a paramagnetic phase with time-dependent sidebands prepares the chiral-spin liquid for cold atoms in PCWs.

In the presence of strong chiral interactions on the triangles Δ of the sublattice, e.g., scalar spin chirality $\hat{\chi}_{\mathrm{scalar}} = \sum_{i,j,k\in\Delta} \vec{\hat{\sigma}}_i \cdot (\vec{\hat{\sigma}}_j \times \vec{\hat{\sigma}}_k)$, the ground state supports a topologically protected chiral edge mode circulating the macroscopic outer boundary with closed loops within the inner hexagons of the kagome lattice [48]. As a convention, the sum $\sum_{i,j,k\in\Delta}$ runs clockwise over the nearest-neighbor sites around the triangles. To see how the extended chiral edge modes emerge in a kagome lattice, we first identify that the ground state of a single closed loop $\hat{\chi}_{\mathrm{scalar}}$ around a single triangle is the Kalmeyer-Laughlin wave function. By mapping the elementary triangular puddles into a Kondo-type network for edge states [48], individual puddles encircled with the chiral states merge together to develop a macroscopic puddle with a single chiral topological edge state around the outer boundary of the lattice, reminiscent of the two-channel Kondo problem. This allows for unidirectional spin transport along the boundary, and the bulk excitations are described by semionic exchange statistics ($\phi = \pi$).

The difficulty in realizing Eq. (8) as the low-energy theory of physical Hamiltonians with cold atoms is the spin-chiral coupling $\vec{\hat{\sigma}}_j \times \vec{\hat{\sigma}}_k$ that breaks the parity symmetry. The capability to realize universal pairwise interaction, including off-diagonal spin operators $\hat{\sigma}_{\alpha}\hat{\sigma}_{\beta}$, makes our approach highly suitable for analog quantum simulation of quantum liquids with chiral-spin coupling. As an example, we realize here the minimal instance of CSL with two-body vector chirality $\hat{\chi}_{\mathrm{vector}} = \sum_{i,j\in\Delta} \hat{z} \cdot (\vec{\hat{\sigma}}^{(i)} \times \vec{\hat{\sigma}}^{(j)})$ in the form of a Dzyaloshinskii-Moriya (DM) interaction. The Raman sideband matrices shown in Figs. 2(b)–(d) realize Eq. (8) on a unit cell of a kagome lattice in Fig. 2(a). The DM interaction breaks the underlying SU(2) symmetry, while preserving the lattice and U(1) spin symmetry. Hence, unlike the case of $\hat{\chi}_{\mathrm{scalar}}$, the CSL does not persist for $\hat{\chi}_{\mathrm{vector}}$ in the limit of strong coupling $\lambda \gg J_{\perp} = J_{ZZ}$. However, it is numerically predicted that the gapped CSL phase does exist for XXZ antiferromagnets with a finite vector spin chirality $\lambda < J_{\perp} = J_{ZZ}$ at zero magnetic field [49,50]. The capability to tune vector chirality as well as other spin-orbit couplings also opens the route to synthetic multiferroics and emergent interfacial spin textures, including skyrmions and topological surface states.

IV. GAUGING THE WAVEGUIDE QED SIMULATOR TO INTERACTING SU(n) LATTICE MODELS

The native Hamiltonian of our waveguide QED simulator spans the universal binary analog models of SU(2)-spin operators. In analogy to lattice gauge theories that give rise to constrained Hilbert space [53,54], we can also design dynamical gauge structures that mediate a wide range of binary models consisting of SU(n) operators in a completely analog fashion, such as the Heisenberg quantum magnet for interacting SU(n) spins. While the digital quantum simulator can emulate the dynamics of arbitrary unitary dynamics, we confine our discussion here to binary SU(n)-spin models that arise within the projected gauge-invariant subspace of the parent's SU(2) waveguide QED simulator. Such a condensed matter approach [53] can create a deconfined quantum phase by direct cooling to its ground state, and the errors can be mitigated within the gauge sector of interest. Indeed, instead of merely replicating the target quantum state as with digital quantum simulators, the actual physical phenomenon is encoded onto the low-energy sector of the waveguide QED simulator. In this section we discuss a general Heisenberg SU(n) quantum magnet as an exemplary implementation, but more complex models involving vector and anisotropy can be realized in an analogous fashion.

Our goal is to create a programmable Heisenberg magnet $\hat{H}_H = \sum_{j>i} \mathcal{J}_{ij} \sum_\alpha \hat{\Lambda}_\alpha^{(i)} \hat{\Lambda}_\alpha^{(j)}$, where $\hat{\Lambda}_\alpha$ is the generalized Gell-Mann matrix (Appendix C 1). The challenge of simulating SU(n) spin with cold atoms and ions is that the spin operators cannot be efficiently mapped to a rotation within an internal DOF due to limited transition pathways, e.g., selection rules. In addition, there is a difficulty in implementing spin models with certain symmetries that cannot be imposed to the fundamental symmetries of the atomic interactions, e.g., SU(n)-symmetric collisions in alkaline-earth atoms limited by the nuclear spin DOF [55]. Apart from the programmability of $\mathcal{J}_{ij}$, the $n^2 - 1$ generators of SU(n) algebra and their interactions would need to be mapped to the physical system. Our method eliminates both bottlenecks, by locally encoding an ensemble of SU(2) spins to the SU(n) subspace and by building the interaction symmetry directly into the Hamiltonian in an emergent manner.

The general strategy is to impose an effective local gauge symmetry onto the spin system through the separation of timescale. We can then introduce a perturbative spin-exchange term that only virtually breaks the local symmetries. By construction, we aim to obtain a microscopic many-body dynamics within the gauge sector, which can be effectively interpreted as the macroscopic binary interactions between the SU(n) spins. From the viewpoint of lattice gauge theories, the constrained quantum dynamics can be qualitatively understood as quantum fluctuations within the background gauge field of a frustrated vacuum of the logical spin system, which give rise to a physical four-body plaquette interaction.

As shown in Fig. 3, we partition the physical atomic lattice i, j into logical spins $\bar{i}, \bar{j} \in \mathcal{L}$, each containing n physical atoms, that encode the local SU(n) spin. This is achieved by local U(1)-gauge constraints $\hat{G}_{\bar{i}}$ that blockade the total excitation number within the logical spin $\bar{i}$ to reside in the single-excitation subspace $\{|\alpha\rangle \equiv |s_\alpha\rangle \prod_{\beta \neq \alpha} |g_\beta\rangle\}$ with $\alpha \in \{1, \dots, n\}$. Such a gauge generator $\hat{G}_{\bar{i}} = \sum_{i \in \bar{i}} \hat{\sigma}_z^{(i)} - \mathcal{Q}$ effectively imposes the Gauss law (ice rules) with electric charge $\mathcal{Q} = n - 2$, analogous to quantum spin ice models [32,53] that mediate long-range ring-exchange interactions. The ground-state (most-excited-state) sector of $\hat{H}_G = \lambda_G \sum_{\bar{i}} \hat{G}_{\bar{i}}^2$ for $\lambda_G > 0$ ($\lambda_G < 0$) is spanned by n-dimensional states $\{|\alpha\rangle\}$ of the SU(n) representation. Without a loss of generality, we rewrite the Heisenberg model within this definition,

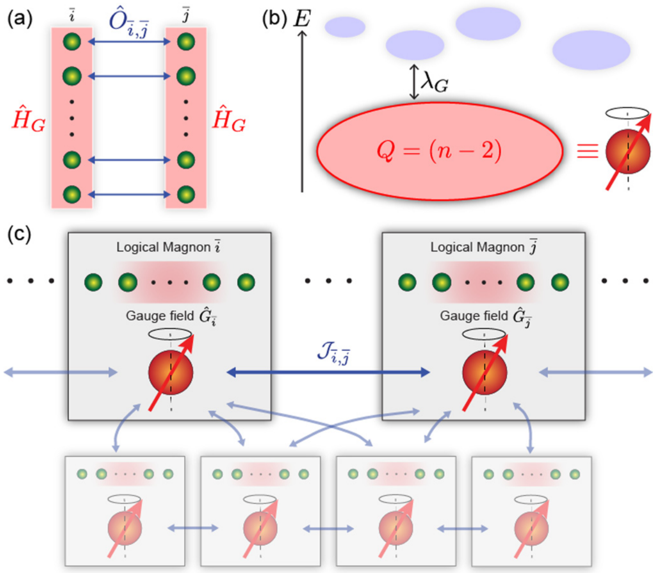

FIG. 3. SU(n)-spin networks under spin ice gauge constraints. (a) Parent spin ice Hamiltonian. Trapped atoms in PCWs are subjected to local ice rules (Gauss laws) with an energetic cost $\hat{H}_G = \lambda_G \sum_{\bar{i}} \hat{G}_{\bar{i}}^2$ within logical blocks $\bar{i}, \bar{j}$. The quantum dynamics among the ice states is induced by a perturbative spin exchange $\hat{O}_{\bar{i},\bar{j}}$ between atoms belonging to different blocks. (b) Effective reduction of the Hilbert space into gauge sectors. The low-energy dynamics is constrained within the SU(n) single-excitation sector, represented by a gauge charge $Q = n - 2$, with errors protected by a many-body gap λ_G. (c) The global spin network is transformed into a network of logical SU(n) spins $\bar{i}$, $\bar{j}$ by encoding the SU(n) spin with a collection of n SU(2) spins. U(1)-gauge constraints $\hat{G}_{\bar{i}}$ block the excitation manifold within the logical spin so that the energy sectors of the parent Hamiltonian are separated by the total excitation number. Spin-exchange coupling between atoms belonging to different logical blocks $\bar{i}$, $\bar{j}$ induces an effective two-body interaction between SU(n) spins.

$$\hat{H}_H = \sum_{\bar{i} \neq \bar{j}} \mathcal{J}_{\bar{i},\bar{j}} \sum_{\alpha,\beta} \hat{\mathcal{T}}_{\alpha\beta}^{(\bar{i})} \hat{\mathcal{T}}_{\beta\alpha}^{(\bar{j})}, \tag{9}$$

where $\hat{\mathcal{T}}_{\alpha\beta} = |\alpha\rangle\langle\beta|$.

In order to introduce spin-spin interaction between the logical blocks, we treat the primitive Hamiltonian $\hat{H}_I = \sum_{\bar{i},\bar{j}} \hat{D}_{\bar{i},\bar{j}} + \hat{O}_{\bar{i},\bar{j}}$ as a perturbation to $\hat{H}_G$ with $\hat{D}_{\bar{i},\bar{j}} = D_{\bar{i},\bar{j}} \sum_\alpha \hat{\sigma}_{ss}^{(\bar{i}_\alpha)} \hat{\sigma}_{ss}^{(\bar{j}_\alpha)}$ and $\hat{O}_{\bar{i},\bar{j}} = O_{\bar{i},\bar{j}} \sum_\alpha \hat{\sigma}_+^{(\bar{i}_\alpha)} \hat{\sigma}_-^{(\bar{j}_\alpha)}$, where $\hat{\sigma}^{(i_\alpha)}$ denotes the spin operator acting on the αth atom in the ith logical block. With the local gauge constraints, we obtain the effective Hamiltonian within the gauge-invariant sector $\mathcal{Q}$ as

$$\hat{H}_{\mathrm{eff}} = \sum_{\bar{i}\neq\bar{j}} D_{\bar{i},\bar{j}} \sum_{\alpha} \hat{\mathcal{T}}^{(\bar{i})}_{\alpha\alpha}\hat{\mathcal{T}}^{(\bar{j})}_{\alpha\alpha} + \mathcal{J}_{\bar{i},\bar{j}} \sum_{\alpha\neq\beta} \hat{\mathcal{T}}^{(\bar{i})}_{\alpha\beta}\hat{\mathcal{T}}^{(\bar{j})}_{\beta\alpha}, \qquad (10)$$

with the gauge-variant errors (spinon excitations) suppressed by the many-body gap λ_G (spinon energy). In the physical space, the spin-exchange coefficients $D_{\bar{i},\bar{j}}, \mathcal{J}_{\bar{i},\bar{j}} = -O^2_{\bar{i},\bar{j}}/2\lambda_G$ are the gauge-mediated ring-exchange interactions among the four spins selected by the primitive two-body model $\hat{H}_I$. With $D_{\bar{i},\bar{j}} = \mathcal{J}_{\bar{i},\bar{j}}$, the effective Hamiltonian is mapped to the universal SU(n) Heisenberg magnet $\hat{H}_H$. The gauge-projected Hamiltonian is derived in Appendix C 2.

One feature of our synthetic approach is that the symmetries of the interaction can be directly built into the underlying Hamiltonian, without resorting to the fundamental symmetries of the atomic collisions. For instance, with a minor modification, we can easily create SU(n)-symmetric Hamiltonians for arbitrary n, e.g., unlimited by the nuclear-spin DOF, for the study of transition metal oxides [56] and heavy fermion systems. Furthermore, because we can design $\mathcal{J}_{\bar{i},\bar{j}}$ arbitrarily through the Raman fields, our system can be tailored to study novel frustrated magnetic ordering in long-range SU(n)-spin models with the Haldane gap [57–60]. As discussed in the next section, our waveguide QED simulator can be applied to the realization of quantum field theories [35,61].

In Appendix C 3 we discuss an efficient method to construct the real-time evolution of the Sachdev-Ye (SY) model [62] with dynamical Raman fields, an all-to-all $\lim_{n\to\infty}$ SU(n) Heisenberg model $\hat{H}_{\mathrm{SY}}$ [Eq. (9) with Gaussian-random $\mathcal{J}_{\bar{i},\bar{j}}$]. The SY model describes a non-Fermi liquid state of matter, known as a "strange metal," characterized by the absence of long-range quasiparticle excitations analogous to high-T_c cuprate superconductors. In connection to quantum chaos [33], a quenched system under $\hat{H}_{\mathrm{SY}}$ rapidly loses the phase coherences and reaches a quantum many-body chaos within timescales that remarkably saturate the quantum bound of the Lyapunov time $\tau_L = \frac{\hbar}{2\pi k_B T}$. With a gauge-mediated many-body string Hamiltonian between a set of SU(n) spins and an ancilla qubit, we can even directly assemble and measure arbitrarily complex out-of-time-order correlators (OTOCs) [63–65] $\langle \hat{W}^\dagger(\tau)\hat{V}^\dagger(0)\hat{W}(\tau)\hat{V}(0)\rangle \sim e^{\tau/\tau_L}$ for SU(n) variables $\hat{W}, \hat{V}$ in our platform for the detection of the quantum chaos and the scrambling of entanglement in many-body quantum systems. The SY model also serves as a model of holography that doubles quantum gravity in 2D anti–de Sitter CFT [33,62].

V. STRONGLY COUPLED WZW FIELD THEORY

Quantum field theories, defined on continuous space-times with each site supporting infinite-dimensional Hilbert spaces, become increasingly intractable to simulate in the regime of strong coupling even on quantum devices. Near the strong coupling, the physics of the UV fixed point is often described by conformal field theories with a scale-invariant and universal description. Moreover, extracting the conformal data of the emergent CFT is a notoriously difficult task for real quantum hardware. In an exemplary fashion, we demonstrate the emergence of (1+1)D SU$(n)_k$ Wess-Zumino-Witten (WZW) CFT [35,61,66] in the waveguide-coupled SU(n) Hamiltonian [Fig. 4(a)], which describes the boundary physics of a bulk (2+1)D Chern-Simons topological gravity in the scaling limit [67]. In condensed matter systems, WZW theory serves as the parent that hosts a family of symmetry-protected gapless edge states in fractional quantum Hall systems. The primary fields Ψ of the CFT are produced and monitored by way of real optical fields of the guided modes. The long-wavelength conformal data, including the central charge c, the quantum dimensions $\mathcal{D}$, and operator product expansion of Ψ, are reconstructed from the correlation between physical observables of the microscopic simulator, as reflected by the fluctuation of the optical fields in the guided mode.

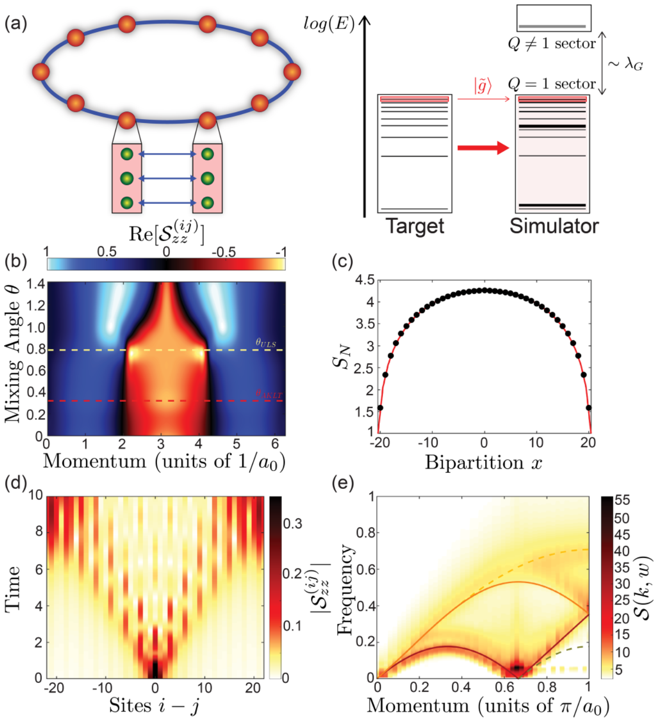

FIG. 4. Emergence of WZW CFT. (a) Local Hamiltonian encoding of SU$(3)_{k=1}$ field theories on a ring onto an SU(2) waveguide QED simulator. The target WZW CFT is isometrically transformed to the local Hilbert space of the simulator with electric charge $Q = 1$. (b) Phase diagram of the bilinear biquadratic spin-1 model with $N_{\mathrm{eff}} = 42$ logical blocks ($N = 124$ atoms). Pinch points of the static structure factor $\mathcal{S}^k_{zz} = \langle S^k_z S^{-k}_z\rangle$ at momentum $k = 2\pi/3, 4\pi/3$ signify the existence of divergent correlations at the ULS QCP. The static structure factor is obtained from the correlation functions in Appendix C 4 with uniform MPSs in the thermodynamic limit. (c) Critical scaling for entanglement entropy for vacuum state of the (1+1)D SU$(3)_k$ WZW field theory of level $k = 1$. The vacuum entanglement entropy follows the Calabrese-Cardy formula for (1+1)D CFTs. The central charge $c = 2.05 \pm 0.03$ is extracted from the finite-size scaling. (d) Production of $c = 2$ primary fields (quasiparticles) upon local quenching. Topological solitons carry fractional quantum statistics of the Abelian anyonic phase $\phi = 2\pi/3$. (e) Dynamical probes for quasiparticles of the WZW CFT. Ground states are obtained with a hybrid DMRG-TEBD algorithm for finite MPSs in a complex-time coordinate (Appendix C 4). The dynamical structure factor is obtained by real-time evolving the ground-state MPS with a TEBD algorithm.

As discussed in Fig. 4(a), we consider a critical SU(3) Heisenberg Hamiltonian for nearest-neighbor interacting N_{eff} logical SU(3) spins existing on a ring with $\mathcal{J}_{\bar{i},\bar{i}+1} = \mathcal{J}_c$ for Eq. (9) [see the phase diagram of Fig. 4(b) with quantum critical point $\theta_{\mathrm{ULS}} = \pi/4$]. The target system is mapped to the waveguide QED simulator (i) by creating nearest-neighbor bonds between physical atoms with $\hat{H}_I$ [blue arrows of Fig. 4(a)] and (ii) by gauging the simulator to $\mathcal{Q}$ [red shaded area of Fig. 4(a)]. The gauged spectrum of the simulator (with λ_G) is thereby that of the target with an error $(D/\lambda_G)^2 \ll 1$. To access the ground state $|\tilde{g}\rangle$ of the target model (most excited state of the gauged simulator), we perform a hybrid matrix-product state (MPS) algorithm for the waveguide quantum simulator moving along a complex time, combining both density-matrix renormalization group (DMRG) and time-evolving block decimation (TEBD) methods. By evolving a random MPS under the action $\lim_{t\to\infty} \exp[-i(\hat{H}_I + i\hat{H}_G)t]$, we obtain the most excited state within the low-energy sector $\mathcal{Q} = 1$ of the simulator, which is isometric to the DMRG ground state of the logical antiferromagnetic SU(3) model (Appendix C 4).

To see how the $\mathrm{SU}(3)_1$ WZW CFT for level $k = 1$ natively emerges from the Hamiltonian constraints of the simulator, let us consider the parton picture of the target Hamiltonian [see Eq. (9)]. We map the logical operators with three-color fermions (quarks) $\hat{\mathcal{T}}^{(\bar{i})}_{\alpha\beta} = \hat{\psi}^{(\bar{i})\dagger}_{\alpha}\hat{\psi}^{(\bar{i})}_{\beta}$ under the constraint $\hat{\psi}^{(\bar{i})\dagger}_{\alpha}\hat{\psi}^{(\bar{i})}_{\alpha} = 1$ for colors $\alpha, \beta = \{r, g, b\}$. The parton Hamiltonian

$$\hat{\mathcal{H}}_{\mathrm{parton}} = \mathcal{J} \sum_{\bar{i}} \hat{\psi}^{(\bar{i})\dagger}_{\alpha}\hat{\psi}^{(\bar{i})}_{\beta}\hat{\psi}^{(\bar{i}+1)\dagger}_{\beta}\hat{\psi}^{(\bar{i}+1)}_{\alpha} \tag{11}$$

is equivalent to an SU(3) Hubbard model $\mathcal{H}_{\mathrm{Hubbard}} = -\sum_{\bar{i}} t[\hat{\psi}^{(\bar{i})\dagger}_{\alpha}\hat{\psi}^{(\bar{i}+1)}_{\alpha} + \mathrm{H.c.}] + U[\hat{\psi}^{(\bar{i})\dagger}_{\alpha}\hat{\psi}^{(\bar{i})}_{\alpha} - 1]^2$ for fermions in the interaction limit $U/t \gg 1$. In the infrared, low-energy excitations are only populated at the Fermi points $k_F = \pi/3$, thereby coarse graining the fermionic fields $\hat{\psi}^{(\bar{i})\dagger}_{\alpha} = e^{ik_F x_{\bar{i}}}\hat{\psi}_{L,\alpha}(x_{\bar{i}}) + e^{-ik_F x_{\bar{i}}}\hat{\psi}_{R,\alpha}(x_{\bar{i}})$ to the continuum. As the Hubbard model for $U/t \ll 1$ gives rise to three-color free Dirac fermions [charge boson and $\mathrm{SU}(3)_1$ WZW gauge fields g], the Hubbard interaction asymptotically decouples the charge with a gap. Thus, the Hubbard interaction leaves the WZW fixed point in the low-energy sector with an action $S = \frac{1}{16\pi}\int_{\mathcal{G}^2} d^2\xi\, \mathrm{Tr}[\partial_\alpha g^{-1}\partial^\alpha g] + \Gamma(g)$ and topological term $\Gamma(g) = \frac{1}{24\pi}\int_{\mathcal{G}^3} d^3\xi\, \epsilon^{\alpha\beta\gamma}\mathrm{Tr}[(g^{-1}\partial_\alpha g)(g^{-1}\partial_\beta g)(g^{-1}\partial_\gamma g)]$. This is reminiscent of chiral Luttinger liquids on fractional quantum Hall edges [68]. Unlike the Haldane phase of the spin-1 counterpart, the emergent field theory of the SU(3) model is described by universal properties, where the (chiral) fermionic fields $\hat{\psi}_{L,\sigma}, \hat{\psi}_{R,\sigma}$ become the Virasoro primary fields $g_{\alpha\beta}(z, \bar{z}) = \hat{\psi}^{\dagger}_{L,\sigma}(z)e^{i\hat{\phi}(z,\bar{z})}\hat{\psi}_{R,\sigma}(\bar{z})$ of the WZW CFT with colors $\sigma = \{r, g, b\}$ and space-time $z = -i(x - t), \bar{z} = i(x + t)$. These fields are generated by the spin currents $J^a_L(x) = \frac{1}{2}\hat{\psi}^{\dagger}_{L,\sigma}(x)\tau^a_{\sigma,\sigma'}\hat{\psi}_{L,\sigma'}(x)$ and $J^a_R(x) = \frac{1}{2}\hat{\psi}^{\dagger}_{R,\sigma}(x)\tau^a_{\sigma,\sigma'}\hat{\psi}_{R,\sigma'}(x)$ following the $\mathrm{SU}(3)_1$ Kac-Moody algebra, where $\tau^a_{\sigma,\sigma'} = (\Lambda_a)_{\sigma,\sigma'}/2$ are the elements of the generalized Gell-Mann matrices in Appendix C 1. Importantly, from the operator product expansion, the conformal data of $\mathrm{SU}(3)_1$ WZW CFT can be obtained for the central charge $c = 2$, scaling dimensions $\mathcal{D} = \frac{2}{3}$, and critical exponents $\nu = 2$ for the WZW field $g_{\alpha\beta}$.

In order to physically extract the conformal data from the simulator, we need to measure the static and dynamic response functions. To this end, we dissipate an observable $\hat{\mathcal{O}}^{(j)}$ of the physical atom at site j to the waveguide $\sum_{\bar{j}} g_{\bar{j}} \sum_{j\in\bar{j}} \hat{\mathcal{O}}^{(j)}\hat{a}_{k_0}e^{ik\bar{j}}$ with a well-defined momentum k. The first-order correlation $\langle{:}\hat{a}^{\dagger}(\tau)\hat{a}(0){:}\rangle_k$ of the optical field leaving the guided mode regresses towards the dynamical response function $\mathcal{S}^k_{\mathcal{O}}(\tau) = \langle 0_{\mathrm{CFT}}|\hat{\mathcal{O}}_{-k}(\tau)\hat{\mathcal{O}}_k(0)|0_{\mathrm{CFT}}\rangle$ of the logical spin system, where $|0_{\mathrm{CFT}}\rangle$ is the vacuum state of the WZW CFT and $\hat{\mathcal{O}}_k = \sum_{\bar{j}} \frac{g_{\bar{j}}}{\kappa_0} \sum_{j\in\bar{j}} \hat{\mathcal{O}}^{(j)}e^{ik\bar{j}}$. This method allows us to construct a broad class of static and dynamical structure factors of the many-body system, giving access to the low-energy excitations as well as the universal properties ν and $\mathcal{D}$ of the CFT. In Appendix C 4 we analyze our result for the spin correlators $\langle \hat{S}^{(\bar{i})}_z \hat{S}^{(\bar{j})}_z \rangle \sim |\bar{i} - \bar{j}|^{-2\mathcal{D}}$ and extrapolate the scaling dimensions $\mathcal{D} = 0.67 \pm 0.02$ with the DMRG ground state up to $N_{\mathrm{eff}} = 200$ logical blocks. We also characterize the correlation length $\xi \sim |\theta - \theta_c|^{-\nu}$ with the critical exponents $\nu = 2.10 \pm 0.05$ for the bilinear biquadratic (BBQ) spin-1 Hamiltonian with the Uimin-Lai-Sutherland (ULS) quantum critical point (QCP) $\theta_c = \pi/4$ with an enlarged SU(3) symmetry, corresponding to our SU(3) Heisenberg model.

In Fig. 4(b) we present the phase diagram of the BBQ model detected with the static spin structure factor $\mathcal{S}^k_{zz} = \langle \hat{S}^{-k}_z \hat{S}^k_z \rangle$. Near the ULS QCP, power-law singularities appear in the form of pinch points at the momenta $k = 2\pi/3$ and $4\pi/3$, indicative of the absence of long-range order (disordered state) for the SU(3)-spin model and the gapless soliton excitations on top of the CFT vacuum (algebraic spin liquid state). These topological solitons appear to carry anyonic statistics with Abelian phase $\phi = \pi$. Upon locally quenching the many-body system with $\hat{S}^{(i)}_z$, these solitons can be produced in pairs moving at the Fermi velocity $v_F = \pi/3$ [Fig. 4(d)]. To assess the spectral properties of WZW fields, we probe the dynamical structure factor $\mathcal{S}_{zz}(w, k) = \int \exp(iw\tau)\mathcal{S}^k_{zz}(\tau)$ in Fig. 4(e). Two soliton modes are visible in the contour map $\mathcal{S}_{zz}(w, k)$ (see the two solid guiding lines), reflected by their length scales $3/2\pi$ and $3/4\pi$. In addition, the solitonic continuum appears smooth as the quasiparticle populations between the two solid lines due the coherence between the soliton pairs, and higher-order 4-local soliton excitations begin to appear between the black dashed line and the red solid line for $k > 2\pi/3$.

We characterize the central charge c of the CFT by scaling the entanglement entropy $S = -\mathrm{Tr}[\rho_A \ln \rho_A]$ between the subsystems A and B of the logical system with $\rho_A = \mathrm{Tr}_B|0_{\mathrm{CFT}}\rangle\langle 0_{\mathrm{CFT}}|$. In the framework of entanglement Hamiltonian $\tilde{H}_A = \sum_l \tilde{\epsilon}_l|\tilde{\epsilon}_l\rangle\langle\tilde{\epsilon}_l|$, we consider the problem of extracting the thermodynamic property of the state $\rho_A = \exp(-\tilde{H}_A) = \sum_l e^{-\tilde{\epsilon}_l}|\tilde{\epsilon}_l\rangle\langle\tilde{\epsilon}_l|$, where $\{\tilde{\epsilon}_l\}$ is the entanglement spectrum for the CFT vacuum state $|0_{\mathrm{CFT}}\rangle$ [69]. The entanglement entropy $S = \sum_l \tilde{\epsilon}_l \ln(\tilde{\epsilon}_l)$ is then obtained from the entanglement Hamiltonian $\tilde{H}_A$ at an effective temperature $T = 1$, whose eigenspectrum $\{\epsilon_l\}$ is determined by many-body spectroscopy [70–72]. Importantly, due to the Bisognano-Wichmann theorem, the entanglement Hamiltonian $\tilde{H}_A$ can be cast in terms of the original model $\hat{H}_H$ [see Eq. (9)] with inhomogeneous coupling $\mathcal{J}_{\bar{i},\bar{i}+1} = \mathcal{J}_c\Gamma(\bar{i})$ and prefactor $\Gamma(x) = \frac{N_{\rm eff}}{\pi}\sin(\frac{\pi x}{N_{\rm eff}})$ defined over a subsystem $\bar{i} \in A$ [69], which can be simulated by the SU(n) toolbox of Eq. (10).

In Fig. 4(c) we present our result of the entanglement entropy for the SU(3) Heisenberg model. At quantum critical points in (1+1) dimensions, the vacuum-state entanglement entropy $S(x, N_{\rm eff})$ logarithmically scales with the system size $N_{\rm eff}$, following the Calabrese-Cardy formula $S(x, N_{\rm eff}) = \frac{c}{3}\log[\frac{N_{\rm eff}}{\pi}\sin(\frac{\pi x}{N_{\rm eff}})]$ for the bipartite cut x up to a nonuniversal offset [73]. By fitting to the Calabrese-Cardy formula, we thereby obtain the central charge $c = 2.05 \pm 0.03$, consistent with the CFT prediction $c = 2$. In the parton theory, the $c = 2$ WZW CFT is manifested by the two-component non-Abelian bosons of the Luttinger liquid. The tensor product of compactified bosons, each carrying $c = 1$ in the dual space, effectively gives rise to the $c = 2$ field theory for the SU(3)-symmetric spin model.

As a final remark, while this section has focused on the minimal instance (1+1)D SU$(3)_1$ WZW CFT, our waveguide QED simulator and measurement protocols are directly applicable to a wider class of WZW CFTs. Namely, the symmetry group SU$(n)_k$ and level k can be engineered with the local encoding $n = N/N_{\rm eff}$ and the sector $\mathcal{Q}$, and long-range interactions can be introduced for arbitrary spatial dimensions. Unlike the Abelian-like spin liquids described by SU$(3)_1$ WZW CFTs, SU$(3)_k$ WZW CFTs are genuinely interacting CFTs and host a far richer family of non-Abelian anyons.

VI. DISCUSSION

Realization of universal quantum matter with a waveguide QED simulator presents technological challenges which can be addressed by state-of-the-art nanophotonic experiments [14–17]. Defect-free atomic arrays can be generated in free space with acousto-optical deflectors [74,75] and spatial light modulators [76]. With evanescent cooling and advanced side-illumination loading techniques for PCW structures [12,77], it is conceivable to prepare a defect-free atom array on flat-band PCWs, such as the SPCW. In Appendix B we provide an example of a SPCW tailored to achieve the desired photonic bands for renormalizing individual Cs atoms to universal quantum matter. Programmable control of the exchange coefficients requires the capability to tune $\sim N^2$ phase amplitudes of the Raman sideband matrices in tandem. Such a capability has been adapted for 100-spin coherent Ising machine [78,79], and ultrafast multimode modulation techniques have been developed in the telecommunication industry. With the present state-of-the-art technologies, it is thus perceivable that the universal quantum matter consisting of several tens of atoms could be realized with the proposed waveguide QED platform. We remark that there is also active research integrating 2D PCWs with cold atoms [80].

In the waveguide QED simulator, the correlated Lamb shift in the PCW generates a mechanical interaction between the external motional states of the trapped atoms. In turn, the Bogoliubov phonons are exploited as a quantum bus for mediating the universal Hamiltonian. Compared to other networked quantum architectures, the PCW allows versatile control over both the dissipative loss and coherent dispersion (single-particle band structure) of such a bus. The figure of merit $\mathcal{F}$ provides a natural scaling parameter for the coherence-to-dissipation ratio of the simulator. In the reactive regime, $\mathcal{F} \sim m_e \exp(L_d/L_c) \gg 1$ exponentially improves with a longer device length L_d for a given photon mass m_e. As an example, in Appendix B we numerically simulate the Green's function $G_{\rm 1D}(\hat{x}_i, \hat{x}_j)$ and find $\mathcal{F} \sim 10^4$ for the silicon nitride SPCW structure.

In conclusion, we have proposed the realization of universal quantum matter with the waveguide QED platform. Compared to previous analog simulation proposals, our platform stabilizes *universal* Hamiltonians that can be adapted to the emulation of arbitrary quantum matter [5]. Physically, our networked approach allows the direct control of the 2-local Hamiltonian $\hat{H}_{\rm QMA}$ at the operator level. Moreover, the static and dynamical structures of arbitrary k-local Hamiltonian $\hat{H}_{\rm target}$ with $k > 2$ of arbitrary dimension can be prescribed to the low-energy theory of the waveguide QED simulator. In particular, we discussed the emergence of programmable binary SU(n) models by gauging the waveguide QED simulator. Indeed, the SU(n) models should be considered as the application of the universality of the simulator, by which the target SU(n) physics is encoded onto the low-energy theory of the waveguide QED simulator. For instance, we have analyzed the paradigmatic quantum field theory, the Wess-Zumino-Witten model by accessing phase diagrams, static and dynamical response functions, and CFT entanglement of the many-body system with matrix-product states.

With respect to digital approaches, the crucial difference is that $\hat{H}_{\rm target}$ is in fact manifested entirely by the waveguide QED simulator. That is, not only the quantum state, but also the entire spectrum of $\hat{H}_{\rm target}$ in tandem is emulated by another physical system. Cooling, thermalization, and the dynamics of the target quantum model can be mapped to the same equilibrium and nonequilibrium physics of the parent analog quantum system. Thus, our approach promises a universal analog quantum simulator, where all physical properties can in principle be replicated as an *emergent* phenomenon.

Waveguide QED offers a unique playground for neutral atoms, in which light, motion, and spin are all intertwined by the electromagnetic vacuum of the dielectric. By engineering the coupling between the phononic superfluid and the atomic spins, we have provided an analog framework for simulating universal quantum matter with cold atoms. Such a simulator can be applied for universal quantum computation with continuous-time quantum cellular automata and Hamiltonian quantum computation [6–8,81]. Our waveguide QED simulator utilizes largely noninteracting phonons with $L_c \gg x_0$. In the limit $L_c \simeq x_0$, the kinetic term of the extended Bose-Hubbard model $\hat{H}_M$ is constrained by the density-density interaction. Under such local gauge symmetries, complex lattice gauge theories beyond truncated quantum link models can emerge from the coherent coupling between the spin matter and fluctuating gauge phonons, renormalizing ordinary noninteracting matter to quantum field theories with the waveguide dielectric.

ACKNOWLEDGMENTS

S. Maurya and A. Boddeti contributed to the numerical simulation of the PCWs. S. G. Weiss of the IQC IST team provided support to the computational cluster. This work was supported by the NSERC, the Canada Foundation for Innovation, the Ontario Ministry of Research and Innovation, NVIDIA, the KIST Institutional Program, the Compute Canada, and the Industry Canada. Y.D. was supported by the Major Scientific Research Project of Zhejiang Laboratory (Grant No. 2019MB0AD01). Y.S.L. was supported by the Mike and Ophelia Lazaridis Fellowship Program.

APPENDIX A: PERFECT TRANSFER IN A SPIN CHAIN

To benchmark and verify the various approximations made for Eq. (6), we simulate a 1D quantum wire that enables perfect quantum-state transfer (QST) between remote spin registers [82–88]. In particular, we compare the effective dynamics of $\hat{H}_{\rm QST}$ to that of the parent Hamiltonian $\hat{H} = \hat{H}_M + \hat{H}_A + \sum_{i,j}\sum_{\alpha,l}\frac{\Omega^{(j)}_{\alpha,l}}{2}\hat{\sigma}^{(i)}_{\alpha}\sin(k^{(j)}_{\alpha,l}\hat{x}_i)e^{-i\nu^{(j)}_{\alpha,l}t} + \text{H.c.}$ in Sec. II A. We prepare a 1D spin medium with the translationally variant XX Hamiltonian

$$\hat{H}_{\rm QST} = \sum_{i=1}^{N-1}\frac{J^{(i,i+1)}}{2}\big(\hat{\sigma}^{(i)}_x\hat{\sigma}^{(i+1)}_x + \hat{\sigma}^{(i)}_y\hat{\sigma}^{(i+1)}_y\big), \tag{A1}$$

where $J^{(i,i+1)} = \alpha\sqrt{i(N-i)}$ and α is a global interaction constant. We solve the system parameters $\{\Omega^{(i)}_{x,k}, \Omega^{(i)}_{y,k}\}$ from the set of nonlinear equations for $J^{(i,i+1)}$ under the constraint of minimum total intensity $\sum_{i,l}(|\Omega^{(i)}_{x,l}|^2 + |\Omega^{(i)}_{y,l}|^2)$.

As discussed in Ref. [82], $\hat{H}_{\rm QST}$ achieves the perfect state transfer of arbitrary input states $|\psi_{\rm in}\rangle$ between the edge sites $i = 1, N$ over arbitrarily long N with unit fidelity by virtue of the mirror symmetry in the spin-exchange coefficients $J^{(i,i+1)}$. Unlike sequential direct state transfer, no external manipulation or feedback on the spin chain is required, and the complete transfer is achieved within transfer time $t_f = \pi/\alpha$ without state preparation of the global spin chain. In Fig. 5(a) we simulate the full Hamiltonian dynamics of quantum-state transfer for two input states $|\psi^{(1)}_{\rm in}\rangle = (|g\rangle - |s\rangle)/\sqrt{2}$ (red solid line) and $|\psi^{(2)}_{\rm in}\rangle = |s\rangle$ (blue dashed line) through a 1D atomic chain with $N = 6$ atoms without eliminating the phonon fields. We keep the coupling terms between those mismatched sidebands and Bogoliubov phonon modes. By sampling various input states coupled to an initially polarized spin medium, the minimal QST fidelity for pure states is numerically determined as $F = \text{Tr}[|\psi^{(1)}_{\rm in}\rangle\langle\psi^{(1)}_{\rm in}|\rho_s] = 0.994$ at $t_f \simeq \pi/\alpha$, yielding only 0.5% error in the final state, testifying to the accuracy of the effective Hamiltonian $\hat{H}_{\rm QMA}$ in Eq. (6).

As shown in the inset of Fig. 5(a), the phonons across the entire spin chain are hardly populated throughout the state transfer, justifying the adiabatic elimination procedure. In Fig. 5(b) we also compare the full atom-phonon dynamics (solid lines) of the individual spin polarizations $\langle\hat{\sigma}^{(i)}_z\rangle$ for an initially polarized spin medium $|g\cdots g\rangle$ with that of the reduced two-body Hamiltonian $\hat{H}_{\rm QST}$ in Eq. (A1) (dashed lines). When $|\psi^{(2)}_{\rm in}\rangle$ is injected to the first spin (black line), the spin excitation delocalizes across the entire spin chain and coherently builds up its amplitude at the final spin with $\langle\hat{\sigma}^{(6)}_z\rangle \simeq 1$ at $t \simeq \pi/\alpha$ (red line). The minute difference between the solid and dashed lines affirms the various approximations for $\hat{H}_{\rm QMA}$. In Appendix B we simulate the full open-system dynamics of QST for Eq. (A1), by starting from the Green's tensor $\boldsymbol{G}(\boldsymbol{x}, \boldsymbol{x}', w)$ of the candidate PCW structure in Fig. 1, and incorporate all known dissipative mechanisms intrinsic to our protocol. Such an effective dynamics is shown to be immune to the structural disorders of the PCW at the tolerance levels of state-of-the-art nanofabrication [89–91].

APPENDIX B: SQUIRCLE PHOTONIC CRYSTAL WAVEGUIDE

The full realization of our waveguide QED toolboxes requires the capability to maintain a favorable figure of merit $\mathcal{F} = \Delta_{\rm Lamb}/\Gamma_{\rm tot}$ with short-range mechanical interactions between the trapped atoms, where the localization length $L_c = \sqrt{1/2m_e\Delta_e}$ is comparable to the lattice constant a_0. Here $\Delta_e \simeq 2\Delta_b$ denotes the detuning of the atomic transition to the effective cavity mode [20] and Δ_b is the detuning of the atomic transition frequency to the band edge. While it is not necessary to have nearest-neighbor interactions with sparse loading, the atomic collective motion can experience a

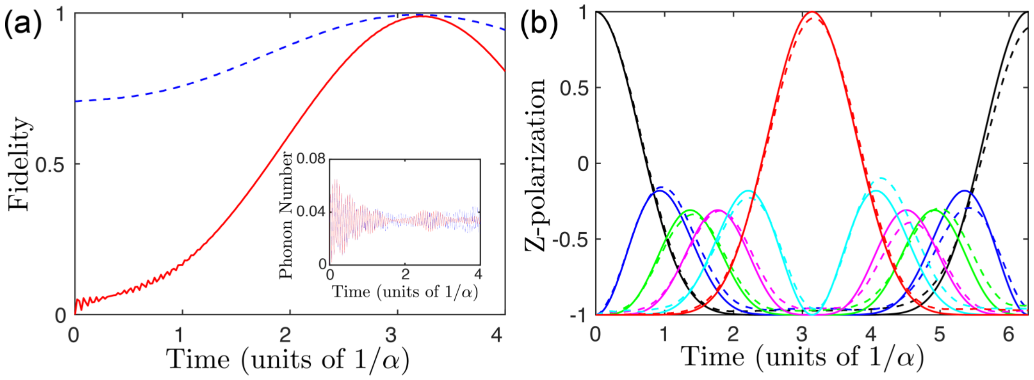

FIG. 5. Quantum-state transfer over a spin chain. (a) Fidelity between the real-time state on the last spin and the initial state on the first spin for two input states $|\psi^{(1)}_{\rm in}\rangle = (|g\rangle - |s\rangle)/\sqrt{2}$ (red solid line) and $|\psi^{(2)}_{\rm in}\rangle = |s\rangle$ (blue dashed line). The inset shows the mean number of phonons with a maximum value about 0.06, which shows that the phonon is rarely populated in the whole process and validates the adiabatic elimination of phonons. The dynamics is numerically simulated for the full Hamiltonian, which includes the interactions of the atomic internal states, phonons, and electromagnetic vacuum. Close-to-unit fidelity $F = 0.994$ is achieved over the timescale $t_f \simeq \pi/\alpha$. (b) Real-time dynamics of spin polarization $\langle\hat{\sigma}_z\rangle$ for all sites on the chain. The dashed (solid) line is obtained from the full (effective) Hamiltonian [in Eq. (A1)].

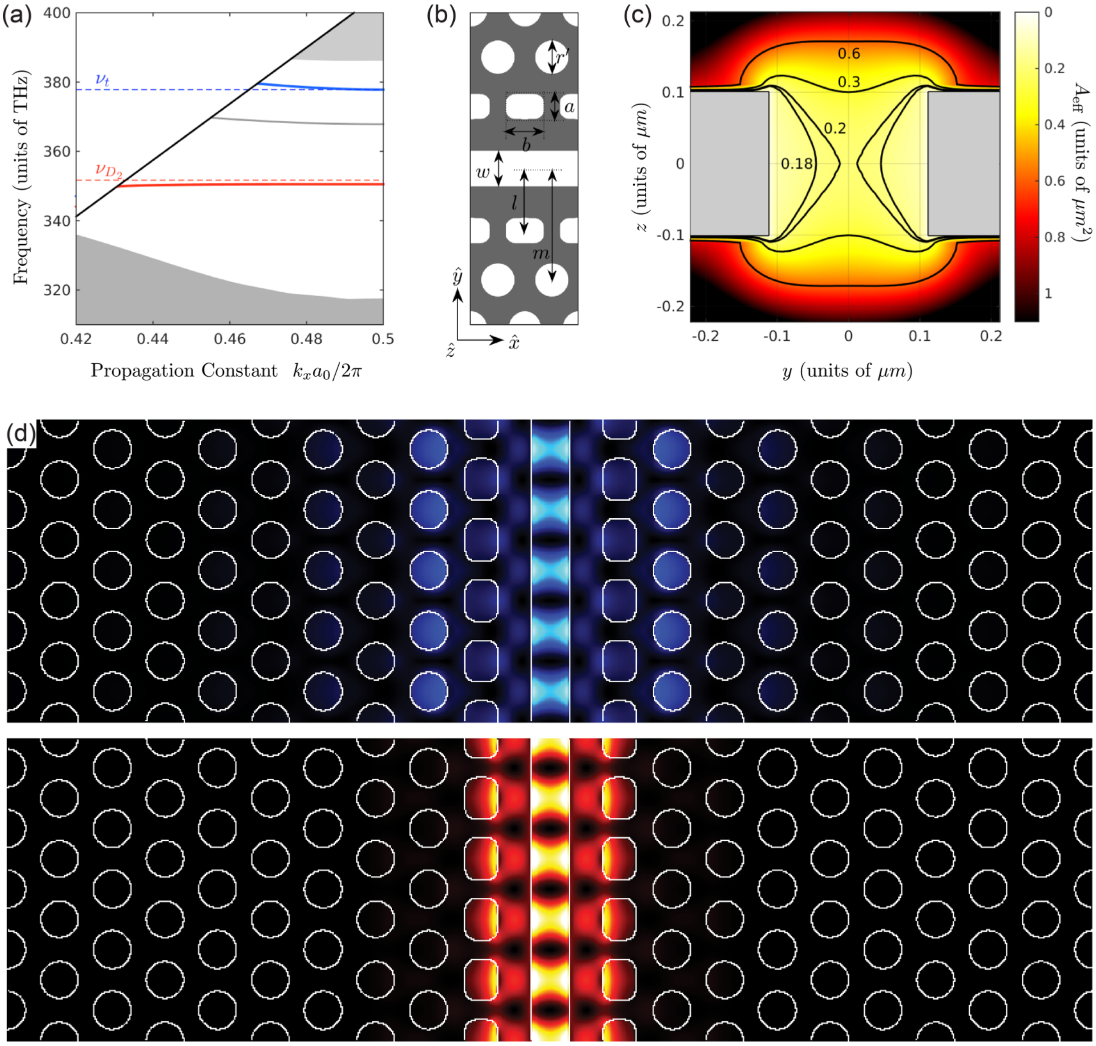

FIG. 6. Slotted squircle photonic crystal waveguide. (a) SPCW band diagram. The guided modes are depicted by solid lines for both the excitationν_{D_2} (red) and trapping modes ν_t (blue). Through our optimization iterations, the GMs ν_{D_2}, ν_t are flattened around the cesium D_2-transition and magic-wavelength trapping frequencies. The GM ν_t is defined to operate at the blue-detuned magic-wavelength condition for the D_2 transition at $\lambda_t = 793.5$ nm. The gray shaded region indicates the presence of slab modes. (b) SPCW geometry. The parameters that define the SPCW structure are provided in Table I. (c) Effective mode area $A_{\rm eff}$. We depict the x-cut contour map of $A_{\rm eff}$ for the GM ν_{D_2}. At the trapping region, we anticipate subwavelength localization $A_{\rm eff}/\lambda_{D_2}^2 \simeq 0.18$ and effective coupling rate $g_c \simeq 11.5$ GHz. The resulting photonic Lamb shift and localization length are $\Delta_{\rm 1D} \simeq 620$ MHz and $L_c \simeq 0.77$ μm at $\Delta_e = 0.4$ THz. (d) Contour intensity map of the guided modes ν_{D_2}, ν_t.

band-flattening effect due to the long-range phonon tunneling, which reduces the local addressability of the spin-motion couplings. For laser cooling and trapping nearby the nanoscopic structures, the PCW requires a wide angular field of view for the optical access and restricts the dimensions of PCW slabs to 1 and 2. Because of the lack of full 3D PBGs, the total decay rate $\Gamma_{\rm tot} = \Gamma_{\rm 1D} + \Gamma'$ consists of both the waveguide decay $\Gamma_{\rm 1D}$ and the homogeneous decay Γ'. While $\Gamma_{\rm 1D}$ is significantly suppressed for large Δ_e, the majority of slow-light PCWs do not have an adequate band structure with large m_e to induce strong coherent motional coupling with $\mathcal{F} \gg 1$ at small L_c.

1. System parameters

In this section we discuss a variation of a slotted PCW that utilizes the PBG of the 2D slab as the guiding mechanism [92–94]. As shown in Fig. 6, the dispersion is tailored by a line defect introduced to a triangular TE PBG slab, where a significant portion of the energy of the GM is localized within the air slot. We introduce anomalous squircles in the vicinity of the air slots to alter their band curvatures. The rationale of our dispersion engineering is that the combination of the lattice constant a_0, the hole radius r, and the air slot width w_s can tune the locations of the band-edge frequencies with respect to the band gap of the slab, while the additional squircle geometries defined by the asymmetry a, b cause differential energy shifts between the z-even bands of opposite x symmetry. By placing the bands deep into the PBG of the surrounding slab, we suppress the k-space interval $[k_c, k_l]$ where the in-plane field profile of the GM is localized by index guiding near the light cone. The proximal squircle geometry then flattens the GM across the band-gap guided k-space fraction $[k_l, k_0]$.

In addition, the out-of-plane emission Γ_h is affected by the distance of the squircles to the slot.

We apply a gradient descent algorithm for the SPCW geometry $n(\vec{r}\,)$ (design variables) to minimize the objective function $F_{\text{total}}(n(\vec{r}\,)) = F_c + F_{D_2} + F_t$ with intermittent thermal excitations to avoid local extrema, as with simulated annealing. The objective function consists of the contributions from band curvature $F_c \propto |m_e|^{-2}$ and frequency deviations $F_{D_2}(F_t) = |\omega_b - \nu_{D_2} + \Delta_b|^2(|\omega_b - \nu_t|^2)$ of $|F=4\rangle \to |F'=5\rangle$ transition frequency ν_{D_2} (blue-detuned magic wavelength frequency ν_t) for atomic cesium from the band edges w_b of the respective modes. During the optimization sequence, the complex band diagram is computed to estimate the effective mass m_e and the localization length L_c with plane-wave expansions [95]. After convergence, we switch over to a finite structure with device length L_d and apply a combination of filter-diagonalized finite-difference time-domain and finite-difference frequency-domain methods [96,97] on a high-bandwidth interconnected computational cluster with the Yee lattice modified to directly optimize the dyadic Green's function $\boldsymbol{G}(\boldsymbol{x}, \boldsymbol{x}', \omega)$ [98,99] and arrive at the final design variable $n(\vec{r}\,)$ in Table I. To include imperfections of realistic devices, we introduce the uncertainty ±1 nm to the system variables consistent with the state-of-the-art PCW nanofabrication techniques [91].

The result of dispersion engineering is shown in Fig. 6(a) for our flat-band silicon nitride SPCW slab, with an effective mass $m_e = 2.1$ Hz^{-1} m^{-2}. In the single-band approximation, the localization length is expected to be $L_c \simeq 2a_0$ at $\Delta_e = 0.4$ THz. We assume that the atom is confined by the blue-detuned magic-wavelength GM trap ν_t at $\lambda_t = 793.5$ nm [blue line in Fig. 6(a)] with the intensity represented by the blue-colored contour map in Fig. 6(d). The excited states of the trapped atom is modified by the vacuum of the ν_{D_2} mode [red line in Fig. 6(a)] as indicated by the red contour map in Fig. 6(d). At the band edge $k_0 = 0.5$, the ν_{D_2} mode is highly localized with the effective mode area $A_{\text{eff}} \simeq 0.18\lambda_{D_2}^2$. The resulting photonic lamb shift is $\Delta_{1\text{D}} \simeq 620$ MHz at $\Delta_e = 0.4$ THz.

We now turn to the numerical Green's function $\boldsymbol{G}(\boldsymbol{x}, \boldsymbol{x}', \omega)$ of a finite SPCW with device length $L_d = 80a_0$ in Fig. 7. We evaluate the collective decay and the coherent interaction

$$\Gamma_{\text{total}}^{(i,j)} = \frac{\mu_0\omega^2}{\hbar}\text{Im}[\boldsymbol{d}^* \cdot \boldsymbol{G}(\boldsymbol{x}_i, \boldsymbol{x}_j, \omega) \cdot \boldsymbol{d}], \tag{B1}$$

$$\Delta_{\text{Lamb}}^{(i,j)} = \frac{2\mu_0\omega^2}{\hbar}\text{Re}[\boldsymbol{d}^* \cdot \boldsymbol{G}_s(\boldsymbol{x}_i, \boldsymbol{x}_j, \omega) \cdot \boldsymbol{d}], \tag{B2}$$

where the scattering Green's function is $\boldsymbol{G}_s = \boldsymbol{G} - \boldsymbol{G}_0$ with respect to the vacuum $\boldsymbol{G}_0$. More generally, we also define the waveguide Green's function $\boldsymbol{G}_{wg} = \boldsymbol{G} - \boldsymbol{G}_h$ absent the homogeneous (nonguided) contributions $\boldsymbol{G}_h$ (coupling to the lossy modes beyond the light cone and to the free-space modes), where the waveguide portion $\boldsymbol{G}_{wg}$ can be estimated from a multimode cavity model [39] under a single-band approximation, with the resulting decay rate

$$\Gamma_{1\text{D}} = \frac{\mu_0\omega^2}{\hbar}\text{Im}[\boldsymbol{d}^* \cdot \boldsymbol{G}_{wg}(\boldsymbol{x}_i, \boldsymbol{x}_j, \omega) \cdot \boldsymbol{d}] \tag{B3}$$

into the waveguide GM.

As shown in Fig. 7, in the dispersive regime [16], the flat band ν_{D_2} exhibits extreme slow-light enhancement of the decay rate with group index $n_g \simeq 1000$ near the band edge. As the atom enters the band gap in the reactive regime $\Delta_e > 0$ [17], the waveguide decay rate $\Gamma_{1\text{D}}$ from $\boldsymbol{G}_{wg}$ is exponentially suppressed [red dashed line in Fig. 7(b)], while the highly asymmetric Fano-like resonance of $\boldsymbol{G}_{wg}$ around the band edge gives rise to a photonic Lamb shift $\Delta_{1\text{D}} \simeq 620$ MHz [Fig. 7(a)] that greatly exceeds $\Gamma_{\text{total}} \simeq 60$ MHz ($\Gamma_{1\text{D}} \simeq 4$ kHz) in the band gap with a figure of merit $\mathcal{F} > 10^4$ at $\Delta_e = 0.4$ THz [Fig. 7(c)], indicating a significant coherence fraction in the collective motion relative to the correlated phononic dissipation. With the close agreement between the numerical Green's function $\boldsymbol{G}$ (black lines) and the waveguide model $\boldsymbol{G}_{wg}$ (red dashed lines) in Fig. 7, we can reliably predict $\Gamma_{1\text{D}}$ from $\boldsymbol{G}_{wg}$ and the mechanical loss factor γ_m from both $\boldsymbol{G}_{wg}$ and $\boldsymbol{G}$. Due to the large value of band flatness, we can operate as close as $\Delta_b = 5$ THz ($\Delta_e \simeq 10$ THz) and attain short-range motional coupling over $L_c \sim 2a_0 \ll L_d$, while maintaining an inherent figure of merit $\mathcal{F} \sim 10^{10}$. We remark that $\mathcal{F}$ is defined as the ultimate coherence-to-dissipation ratio for the collective phonon modes in Sec. II A, where we only consider the inherent dissipation of the atomic motions in the photonic band gap. In practice, our method will be realistically limited by the phase noises of Raman sideband lasers and the inhomogeneous hyperfine broadening of the trapped atoms, as well as various uncontrollable surface forces.

For disordered photonic structures, we compute the dyadic Green's functions with the Gaussian random geometric disorder ∼1 nm (positions and sizes of the holes and thickness of the waveguide) distributed across the entire nanophotonic waveguide. In a single realization, the radiative enhancement factor at the band edge may be hindered by Anderson and weak localization. However, in the reactive regime $\Delta_e > 0$, we observe that the decay rate and the photonic Lamb shift in Fig. 7, as well as the nonlocal Green's function $\boldsymbol{G}(\boldsymbol{x}_i, \boldsymbol{x}_j, \omega)$, are not significantly modified by the structural disorders ∼1 nm (gray dashed lines in Fig. 7). Such nanofabrication tolerances have been demonstrated in Refs. [15,17]. Because of the nature of the photonic band gap, the nonradiative atom-field localized modes are resistant to the degree of structural disorder.

2. Ground-state potentials and phononic modes

We now turn our attention to the trapping mechanism for the atoms in the SPCW. To form an atomic chain, we confine the atoms in the y-z plane by two incoherent side-illumination (SI) beams [13,16] and localize the x motion by a weak GM trap at 794 nm, as shown in Fig. 8. With the SI beams near the blue-detuned magic wavelength $\lambda = 687$ nm in an optical accordion, we anticipate efficient loading into the GM trap. Because the SI beam provides additional confinement along z [100–102], we can operate the GM trap away from the band edge at $k_x = 0.48$, thereby reducing the intensity contrast along x. With this protocol we can gain a 3D far-off-resonance trap (FORT) with trapping potential shown in Figs. 8(d)–8(f).

From the numerical nonlocal Green's function $\boldsymbol{G}(\boldsymbol{r}_i, \boldsymbol{r}_j, w)$, we observe that the localization length scales with $L_c = \sqrt{1/2m_e\Delta_e}$ and the effective mass $m_e = 2.1$ Hz^{-1} m^{-2} up

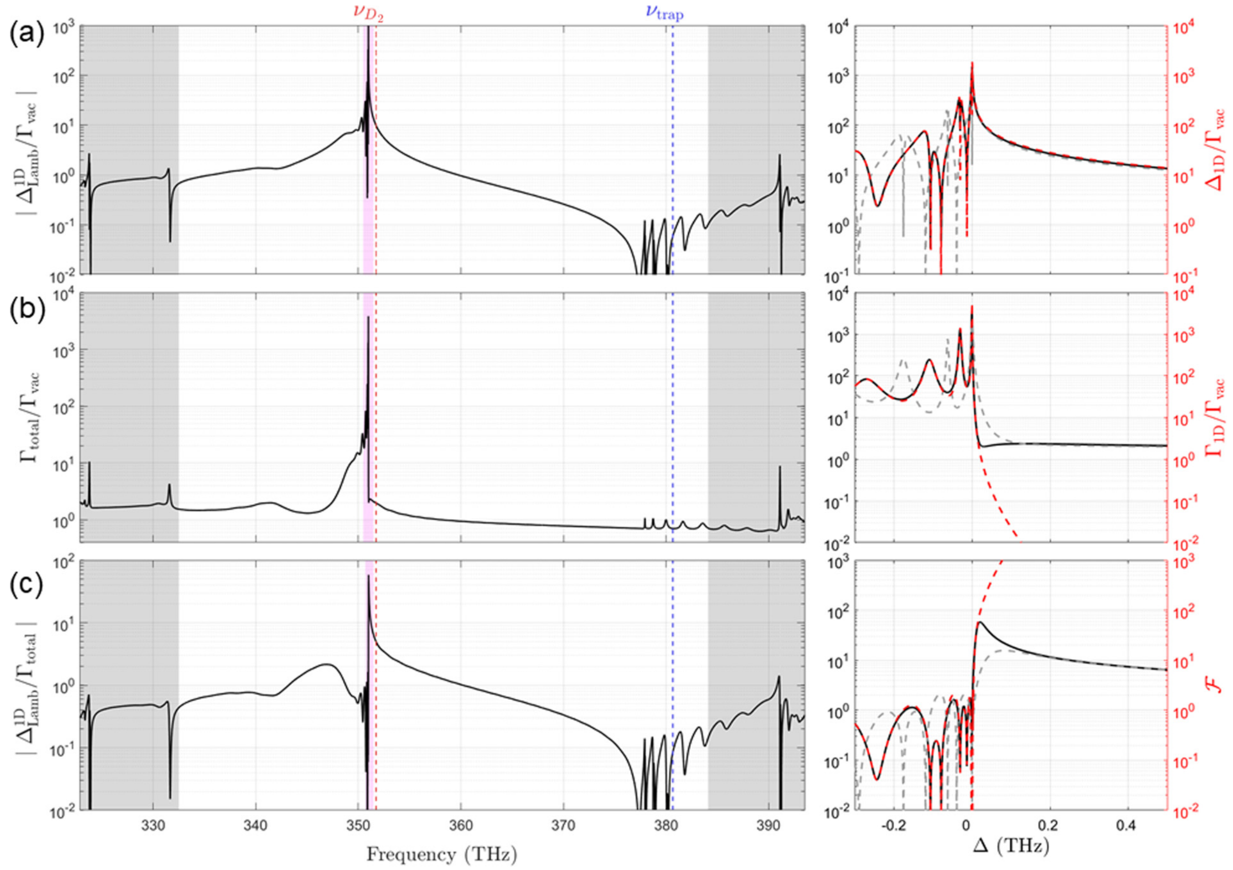

FIG. 7. Collective atomic decay and photonic Lamb shift of a finite SPCW. (a) Photonic Lamb shift $\Delta^{\rm 1D}_{\rm Lamb}$ for electronically excited states. The energy shift $\Delta_{\rm 1D}$ of the excited state $|6P_{3/2}, F = 4\rangle$ of Cs is computed by numerically evaluating the local scattering Green's function $\boldsymbol{G}_s(\boldsymbol{x}, \boldsymbol{x}', \omega)$. We only consider the level shift caused by the SPCW structure, but not the absolute renormalization by the electromagnetic vacuum. As a benchmark, we normalized the Lamb shift by the free-space decay rate $\Gamma_{\rm vac}$. We also display the photonic Lamb shift $\Delta_{\rm 1D}$ under the single-band approximation as a red dashed line. The close agreement between the two models testifies to the accuracy of the extrapolated $\Gamma_{\rm 1D}$. (b) Enhancement and inhibition of spontaneous emission in dispersive and reactive regimes. The total decay rate $\Gamma_{\rm total}$ is strongly enhanced at the band edge and is exponentially inhibited in the band gap with $\Gamma_{\rm total} \simeq \Gamma_{\rm 1D} \exp(-L_d/L_c)$, where $\Gamma_{\rm 1D}$ is the enhanced decay rate at the resonance closest to the band edge, $L_d = 80a_0$ is the device length for lattice constant a_0, and L_c is the localization length. Deep into the band gap $\Delta_e \gg 0$, the reduction of $\Gamma_{\rm total}$ is limited by the weakly inhibited homogeneous decay rate $\Gamma' \simeq 0.7\Gamma_{\rm vac}$ that predominantly emits photons out of plane of the slab. (c) Lamb shift to decay rate ratio $\Delta_{\rm 1D}/\Gamma_{\rm total}$ across a wide detuning range up to $\Delta_e \simeq 10$ THz. The inset shows the figure of merit $\mathcal{F} \gg 1$ (red dashed line). The gray shaded region indicates the presence of slab modes.

to $\Delta_e \simeq 5$ THz. We attribute the deviation of the localization scaling beyond $\Delta_e > 5$ THz to the residual Lamb shift by the off-resonance couplings to the other bands and to the slab modes. Figure 9 depicts the local nature of external atom-atom interaction $t_{ij} = \eta_l^2 f^2 \Delta_{\rm Lamb}(x_i, x_j)$ with $\eta_l = x_0/L_c$ relative to the mechanical decoherence $\gamma_m = \eta_l^2 f^2(\Gamma_{\rm 1D} + |\Delta_{\rm Lamb}/\Delta_e|^2\Gamma')$, where the homogeneous decay rate $\Gamma' \simeq 0.7\Gamma_{\rm vac}$ is weakly inhibited. At $\Delta_e = 0.4$ THz, we find the tunneling rate $t \simeq 2\pi \times 230$ kHz, localization length $L_c = 0.77$ μm, and phonon loss rate $\gamma_m \simeq 2\pi \times 5$ Hz. Another possible error source could be recoil heating from the trapping beam. Since we work with FORT in blue detuning, the heating rate can be estimated as $\gamma_{\rm heat} \simeq E_r(\Omega_t/\delta_t)^2\Gamma'/\hbar w_t$ [103], where Ω_t and δ_t are the trapping Rabi frequency and laser-atom detuning, respectively, and $E_r = 4\pi^2\hbar^2/2m\lambda_t^2$ is the recoil energy. For the cesium atom and our trapping setup, the heating rate is estimated as $\gamma_{\rm heat} \sim 0.2$ Hz $\ll \gamma_m$ and therefore can be neglected safely. (See Table II).

Beyond the scope of the present work, we have also investigated SPCWs with strong phononic on-site U_0 interactions, which map the phononic model to the XXZ spin magnet and Luttinger liquids for finite filling factor. Further design variation that provides strong phononic density-density interaction $U_{ij}\hat{n}_i\hat{n}_j$ will be discussed elsewhere. Such a constraint on the local phonon field provides a mechanism to impose local symmetry similar to the context of lattice gauge theories in condensed matter systems.

3. Phonon-mediated spin-exchange coefficient

For universal spin control with $N \simeq 50$ atoms, we estimate the spin-exchange coupling rate $J_{ij} \simeq 50$ kHz with the intrinsic decoherence rate $\gamma^{(i,j)}_{\alpha,\beta} \ll 1$ Hz at $\Delta_e = 0.4$ THz. As an example, we depict the open-system dynamics of the quantum-state transfer protocol in Fig. 10 by solving the master equation [Eqs. (6) and (7)]. As discussed above, because of $\gamma_m/\Delta_M \sim 10^{-4}$, the intrinsic phonon-induced spin

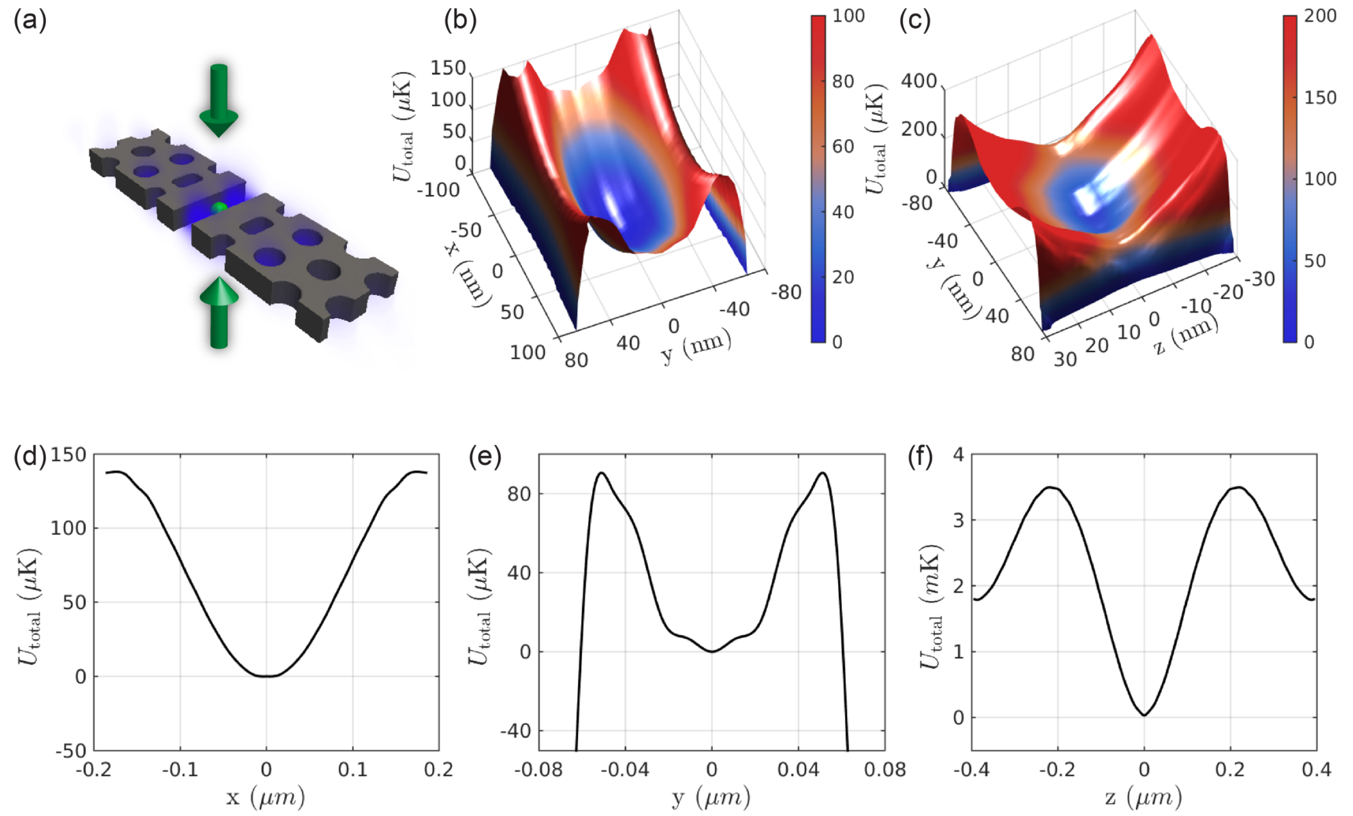

FIG. 8. Adiabatic ground-state potentials for the cesium atom assisted by side-illumination beams. Cesium trapping potentials of $|6S_{1/2}\rangle$ are plotted in (b) the x-y plane and (c) the y-z plane with the (d) x, (e) y, and (f) z slices. We assume that the refractive index n is frequency independent. The coordination system (x, y, z) of the SPCW is defined in Fig. 6(b).

decoherence $\gamma_{\alpha,\beta}^{(i,j)}$ is highly negligible. We thereby include the spin-relaxation rate $\gamma_{\text{FORT}}^{(i,i)} < 1$ Hz of the FORT beams [104] by adding the following local dissipative terms to the original master Eq. (7):

$$\mathcal{L}_{ss}[\hat{\rho}_S] = -\sum_i \frac{\gamma_{\text{FORT}}^{(i,i)}}{2}(\{\hat{\sigma}_{ss}, \hat{\rho}_S\} - 2\hat{\sigma}_{gs}\hat{\rho}_S\hat{\sigma}_{sg}),$$

$$\mathcal{L}_{gg}[\hat{\rho}_S] = -\sum_i \frac{\gamma_{\text{FORT}}^{(i,i)}}{2}(\{\hat{\sigma}_{gg}, \hat{\rho}_S\} - 2\hat{\sigma}_{sg}\hat{\rho}_S\hat{\sigma}_{gs}).$$

We note that, due to the highly differential decay rates for theD_1 and D_2 lines of Cs by the SPCW, we do not observe any suppression of Raman spontaneous emission rates relative to the Rayleigh scattering by the FORT. The state fidelities for $N = 1$ and $N = 6$ atoms are displayed as black and red solid lines in Fig. 10, respectively. We assume an initially injected spin state of $|s\rangle$ with the parameters of Fig. 5. For the clarity of presentation, the remaining spin medium is prepared in the ground state $|g \cdots g\rangle$. As the spin excitation is transferred within the dissipative spin chain, the overall spin medium is thermally depolarized by the actions of the local dissipation and the state fidelity F is progressively reduced to $F \to 0.5$ with $\hat{\rho}_S \to \prod_i \frac{1}{2}(|g_i\rangle\langle g_i| + |s_i\rangle\langle s_i|)$.

APPENDIX C: SU(n)-GAUGE WAVEGUIDE QED SIMULATOR

1. Generalized Gell-Mann matrices

The n-dimensional Hermitian generalized Gell-Mann matrices (GGMs) are the higher-dimensional extensions of the Pauli matrices (for qubits) and the Gell-Mann matrices (for qutrits). Similar to the roles the Pauli (Gell-Mann) matrices play in SU(2) [SU(3)] algebra, they are the standard SU(n) generators. There are three different types of GGMs, $\frac{n(n-1)}{2}$ symmetric ones, $\frac{n(n-1)}{2}$ antisymmetric ones, and $n-1$ diagonal ones, which are defined respectively as follows: symmetric GGMs ($1 \leqslant \alpha < \beta \leqslant n$)

$$\hat{\Lambda}_{\alpha\beta}^{(s)} = |\alpha\rangle\langle\beta| + |\beta\rangle\langle\alpha|, \tag{C1}$$

antisymmetric GGMs ($1 \leqslant \alpha < \beta \leqslant n$)

$$\hat{\Lambda}_{\alpha\beta}^{(a)} = -i|\alpha\rangle\langle\beta| + i|\beta\rangle\langle\alpha|, \tag{C2}$$

and diagonal GGMs ($1 \leqslant \alpha \leqslant n-1$)

$$\hat{\Lambda}_{\alpha\alpha}^{(d)} = \sqrt{\frac{2}{\alpha(\alpha+1)}}\sum_{\beta=1}^{\alpha} |\beta\rangle\langle\beta| - \alpha|\alpha+1\rangle\langle\alpha+1|. \tag{C3}$$

Hence, in total, we have $n^2 - 1$ GGMs. From the definitions, one can verify that, similar to the Pauli matrices, all GGMs are Hermitian and traceless. They are orthogonal and form a basis together with identity $\hat{I}_n$.

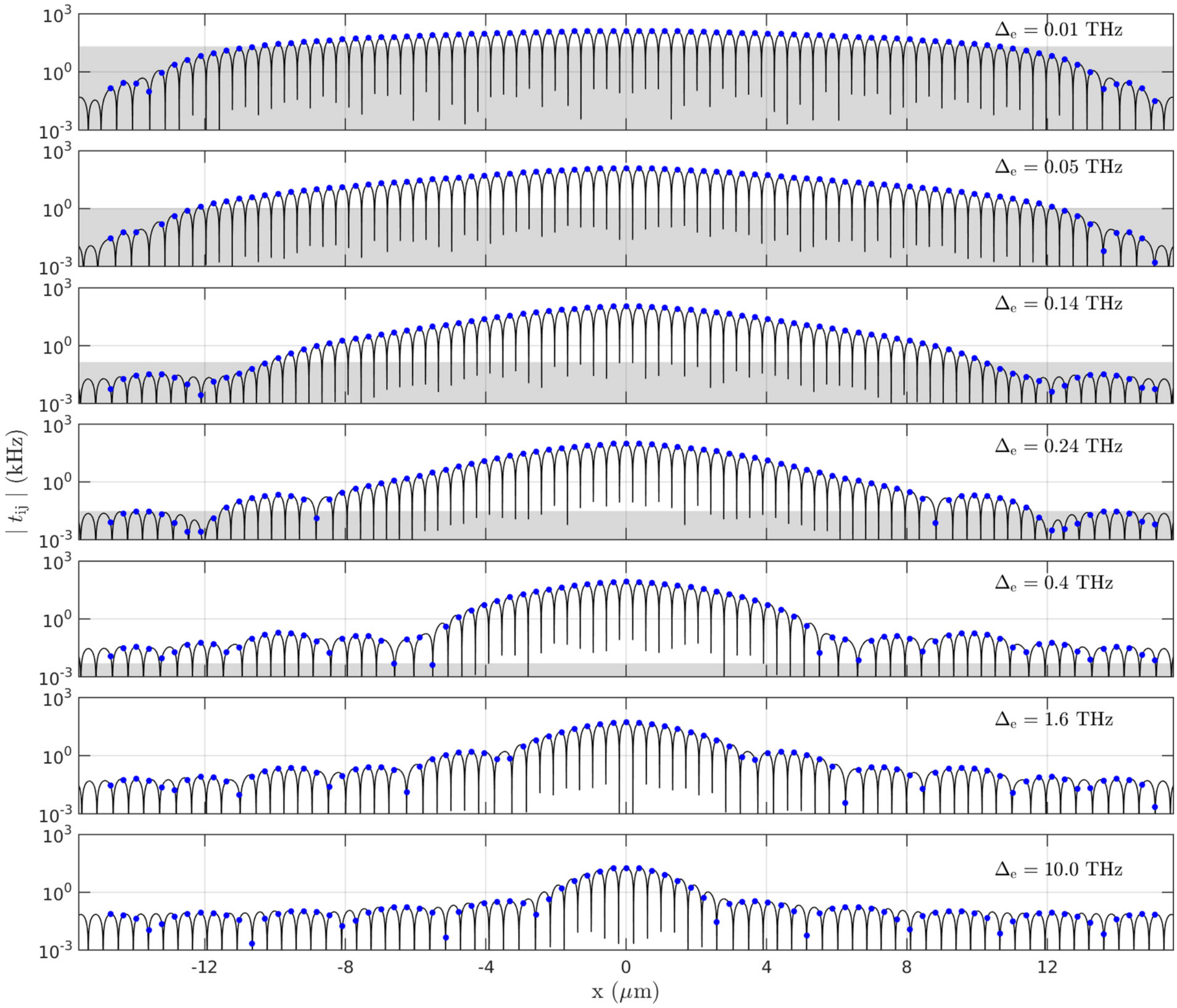

FIG. 9. Short-range atom-atom interaction in a photonic band gap. We numerically evaluate the nonlocal Green's function $\boldsymbol{G}(\boldsymbol{x}_i, \boldsymbol{x}_j, w)$ for the SPCW and obtain the figure of merit for effective detunings $\Delta_e = 0.01, 0.05, 0.14, 0.24, 0.4, 1.6, 10$ THz. Due to the large photon mass m_e, the atoms experience exponentially localized tunneling interactions $t_{ij}/\gamma_m \gg 1$ over lengths L_c. The gray shaded regions depict the dissipative regime with $t_{ij} < \gamma_m$, where collective phononic loss dominates over the coherent tunneling rate. For large Δ_e, the ratio $t_{ij}/\gamma_m \gg 10^4$ is exponentially enhanced at the expense of reduced values $t_{ij} \simeq 2\pi \times 20$ kHz and localized length $L_c \simeq 2.5a_0$ at $\Delta_e \simeq 10$ THz.

2. Gauge-projected SU(n) Heisenberg model

To gauge the primitive Hamiltonian $\hat{H}_I$ to the local symmetry sector, we define a projection operator $\hat{P}_G$ which brings quantum states to the ground-state sector $\mathcal{Q} = n - 2$ of the gauge Hamiltonian $\hat{H}_G$, namely, $\hat{H}_G\hat{P}_G = \hat{P}_G\hat{H}_G = E_G\hat{H}_G$, where E_G is the ground-state energy of $\hat{H}_G$. We perturbatively expand $\hat{H}_I$ within the sector $\mathcal{Q}$ with the Kato series

$$\begin{aligned}\hat{H}^{(1)}_{\text{eff}} &= \hat{P}_G\hat{H}_I\hat{P}_G,\\ \hat{H}^{(2)}_{\text{eff}} &= \hat{P}_G\hat{H}_I\hat{S}_{k1}\hat{H}_I\hat{P}_G,\\ \hat{H}^{(3)}_{\text{eff}} &= \hat{P}_G\hat{H}_I\hat{S}_{k1}\hat{H}_I\hat{S}_{k2}\hat{H}_I\hat{P}_G,\\ &\vdots\end{aligned}$$

TABLE II. Summary of energy scale hierarchy and corresponding effective error rates.

Energy hierarchy	Expression	Requirements	Typical value	Effective error source	Expression	Typical value
Atom-PCW ww interaction	$g_c \simeq \sqrt{\frac{\omega_b d^2}{2\epsilon_0 A_{\text{eff}} L_c}}$		~10 GHz	Photon loss	$\kappa \simeq \kappa_0 \exp\left(-\frac{L_d}{L_c}\right) + \frac{g_c^2}{\Delta_e^2}\Gamma'$	~10 MHz
Mechanical tunneling	$t_{ij} \simeq \eta_l^2 g_m$	$f \ll 1$	~1 MHz	Phonon loss	$\gamma_m \simeq \frac{\eta_l^2 g_m}{\Delta_e}\kappa$	~10 Hz
Spin-spin interaction	$J^{(i,j)}_{\alpha,\beta} = 2\,\text{Re}\left[\frac{\tilde{\Omega}^{(i)}_{\alpha,l}\tilde{\Omega}^{(j)*}_{\beta,l}}{\Delta_M}\right]$	$\lvert\tilde{\Omega}^{(i)}_{\alpha,l}\rvert \ll \Delta_M \ll \lvert\epsilon_{l\pm1} - \epsilon_l\rvert$	~50 kHz	Spin decoherence	$\gamma^{(i,j)}_{\alpha,\beta} \simeq \frac{\gamma_m}{\Delta_M} J^{(i,j)}_{\alpha,\beta}$	~0.1 Hz

where $\hat{S}_0 = -\hat{P}_G$ and $\hat{S}_n = [(1-\hat{P}_G)(E_G - \hat{H}_G)^{-1}]^n$. Because $\hat{H}_I$ breaks the local gauge symmetry, the first-order term vanishes $\hat{H}_{\text{eff}}^{(1)} = 0$. The low-energy dynamics is thereby described at the second order with

$$\hat{H}_{\text{eff}}^{(2)} = \sum_{\bar{i},\bar{j}} \mathcal{J}_{\bar{i},\bar{j}} \left(\sum_{\alpha\neq\beta} \hat{\sigma}_{+}^{(\alpha,\bar{i})} \hat{\sigma}_{-}^{(\beta,\bar{i})} \hat{\sigma}_{+}^{(\beta,\bar{j})} \hat{\sigma}_{-}^{(\alpha,\bar{j})} \prod_{k\neq\beta} \hat{\sigma}_{gg}^{(k,\bar{i})} \prod_{l\neq\alpha} \hat{\sigma}_{gg}^{(l,\bar{j})} + \hat{\sigma}_{ee}^{(\alpha,\bar{i})} \hat{\sigma}_{ee}^{(\beta,\bar{j})} \prod_{k\neq\alpha} \hat{\sigma}_{gg}^{(k,\bar{i})} \prod_{l\neq\beta} \hat{\sigma}_{gg}^{(l,\bar{j})} + \text{H.c.} \right), \tag{C4}$$

where the ring-exchange coefficient $\mathcal{J}_{\bar{i},\bar{j}} = -O_{\bar{i},\bar{j}}^2/2\Lambda_G$ is mediated by a pair of virtual spinon excitations $\mathcal{Q}' = \mathcal{Q} \pm 2$. By the addition of a gauge-invariant two-body Hamiltonian $\hat{H}_{\text{anc}} = -\sum_{\bar{i},\bar{j}}(\mathcal{J}_{\bar{i},\bar{j}} \sum_{\alpha\neq\beta} \hat{\sigma}_{ee}^{(\alpha,\bar{i})}\hat{\sigma}_{ee}^{(\beta,\bar{j})} + \mathcal{D}_{\bar{i},\bar{j}} \sum_{\alpha} \hat{\sigma}_{ee}^{(\alpha,\bar{i})}\hat{\sigma}_{ee}^{(\alpha,\bar{j})})$ to the perturbative Hamiltonian $\hat{H}_{\text{total}} = \hat{H}_{\text{anc}} + \hat{H}_{\text{eff}}^{(2)} + \hat{H}_G$, we obtain the effective Hamiltonian in Eq. (10) within the single-excitation gauge sector $\mathcal{Q}$.

3. Sachdev-Ye quantum magnet

In Sec. IV we discussed the all-to-all connected SU(n) Heisenberg model. However, as an effective model in terms of second-order perturbation, all connections $\mathcal{J}_{ij}$ must be all negative (ferromagnetic) or positive (antiferromagnetic), determined by the eigenenergy sector that we choose, while fully Gaussian randomly distributed couplings are the crucial ingredients for the generation of quantum chaos of the Sachdev-Ye (SY) model [33,62]. The SY Hamiltonian reads

$$\hat{H}_{\text{SY}} = \frac{1}{\sqrt{n}} \sum_{j>i} \mathcal{J}_{ij} \sum_{\alpha} \hat{\Lambda}_{\alpha}^{(i)} \hat{\Lambda}_{\alpha}^{(j)}, \tag{C5}$$

where the after-quench connections $\{\mathcal{J}_{ij}\}$ are drawn from the probability distribution $P(\mathcal{J}_{ij}) \sim \exp(-\mathcal{J}_{ij}^2/2\mathcal{J}^2)$.

We describe a stroboscopic strategy to simulate the dynamics driven by such a Hamiltonian. For an arbitrary SY Hamiltonian, we can separate it into two parts $\hat{H}_{\text{SY}} = \hat{H}_{\text{SY}}^{(+)} + \hat{H}_{\text{SY}}^{(-)}$, where $\hat{H}_{\text{SY}}^{(+)}$ ($\hat{H}_{\text{SY}}^{(-)}$) contains only all terms with positive (negative) connections and thus can be realized efficiently in our platform. To realize a coarse-grained unitary evolution in a single time step Δt, we first turn on the positive Hamiltonian $\hat{H}_{\text{SY}}^{(+)}$ for a time period of $\Delta t/2$. Then we switch on the $\hat{H}_{\text{SY}}^{(-)}$ for the same period and keep the Hamiltonian for another Δt. Finally, we evolve the system again under $\hat{H}_{\text{SY}}^{(+)}$ for $\Delta t/2$. The entire dynamics is then given by $\exp(-i\hat{H}_{\text{SY}}\Delta t) + O(\Delta t^3)$ with an error of the order Δt^3 due to the noncommuting $\hat{H}_{\text{SY}}^{(+)}$ and $\hat{H}_{\text{SY}}^{(-)}$.

We can also measure the out-of-time-operator correlations for the SY model in our platform, which is essential for describing the entanglement scrambling in this system. The crucial step is creating a controlled GMM operation $\hat{U}_{C\text{-}\Lambda_\alpha} = |g\rangle\langle g| \otimes \hat{I} + |s\rangle\langle s| \otimes \hat{\Lambda}_\alpha$, which can be used to decompose an arbitrary SU(n) operator. Let us take a controlled symmetric GGM C-$\hat{\Lambda}_{\alpha\beta}^{(s)}$ as an example. To realize this kind of controlled operations, we can couple an ancilla qubit to the αth and the βth qubits in a single logical block with the two-body term $\hat{H}_{\alpha\beta} = \chi_\alpha \hat{\sigma}_{ss}^{(\mathcal{A})}\hat{\sigma}_{+}^{(\alpha)} + \chi_\beta \hat{\sigma}_{ss}^{(\mathcal{A})}\hat{\sigma}_{+}^{(\beta)} + \text{H.c.}$ This leads to an effective interaction $\tilde{\chi}_{\alpha\beta}\hat{\sigma}_{ss}^{(\mathcal{A})}\hat{\mathcal{T}}_{\alpha\beta} + \text{H.c.}$ within the gauge-invariant sector $\mathcal{Q}$, where $\tilde{\chi}_{\alpha\beta} = \chi_\alpha^* \chi_\beta/\lambda_G$, with λ_G is the coupling constant in gauge Hamiltonian $\hat{H}_G$ defined in Sec. IV. According to the definition of GGMs, if $\tilde{\chi}_{\alpha\beta}$ is real, the evolution under this Hamiltonian for an interaction time $t = \pi/2|\tilde{\chi}_{\alpha\beta}|$ yields $\hat{U}_{C-\Lambda_{\alpha\beta}^{(s)}}$. Furthermore, if we set $\tilde{\chi}_{\alpha\beta}$ as pure imaginary, a controlled antisymmetric GGM C-$\hat{\Lambda}_{\alpha\beta}^{(a)}$ would be realized.

We next describe a general method to construct and efficiently measure OTOCs for arbitrary SU(n) observables in this system driven by arbitrary Hamiltonian $\hat{H}_{\text{SY}}$ without tomographic reconstruction. Unlike other protocols, our strategy is to encode the OTOC onto the single ancilla qubit $\mathcal{A}$ through controlled string operation and interferometrically read out the internal state of a *single* ancilla qubit. We consider two operators $\hat{V}^{(i)} = \sum_\alpha v_\alpha^{(i)}\hat{\Lambda}_\alpha^{(i)}$ and $\hat{W}^{(j)} = \sum_\beta w_\beta^{(j)}\hat{\Lambda}_\beta^{(j)}$ acting on the system logical magnons and decomposed by the GGM operators $\{\hat{\Lambda}_\alpha^{(i)}\}$ and $\{\hat{\Lambda}_\beta^{(i)}\}$. The goal is then to measure all $C_{\alpha,\beta,\alpha',\beta'} \equiv \langle \hat{\Lambda}_{\beta'}^{(j)}(\tau)\hat{\Lambda}_{\alpha'}^{(i)}(0)\hat{\Lambda}_{\beta}^{(j)}(\tau)\hat{\Lambda}_{\alpha}^{(i)}(0)\rangle$ and construct the overall OTOC with weighted distribution $w_{\beta'}^* v_{\alpha'}^* w_\beta v_\alpha$. The circuit in Fig. 11 facilitates the transformation that maps the dynamical correlators $C_{\alpha,\beta,\alpha',\beta'}$ to the ancilla qubit with the initial system-ancilla state $|\psi(0)\rangle_{\mathcal{S}} \otimes |g\rangle_{\mathcal{A}}$. The ancilla atom can be physically represented by the atoms in close proximity to the impedance-matching tethers of PCWs, so that the internal spins of the ancilla atom can readily dissipate evanescently to the input and output couplers. The sequence of gate sets maps the initial state to $\hat{V}_{\alpha'}^{(i)}(0)\hat{W}_{\beta'}^{(j)}(\tau)|\psi(0)\rangle_{\mathcal{S}}|s\rangle_{\mathcal{A}} + \hat{W}_{\beta}^{(j)}(\tau)\hat{V}_{\alpha}^{(i)}(0)|\psi(0)\rangle_{\mathcal{S}}|g\rangle_{\mathcal{A}}$ with $\hat{O}(\tau) = e^{i\hat{H}\tau}\hat{O}e^{-i\hat{H}\tau}$. Here the time-inverse evolution can be realized in a positive time flow but inverse the sign of all $\mathcal{J}_{ij}$. As with Ramsey interferometer, we measure the expectation values of the local spin vectors for qubit $\mathcal{A}$, where the dynamic correlators of the system atoms are $C_{\alpha,\beta,\alpha',\beta'} = \frac{1}{2}[\langle\hat{\sigma}_x\rangle_{\mathcal{A}} + i\langle\hat{\sigma}_y\rangle_{\mathcal{A}}]$. This method can be extended to high-order dynamic correlations in a straightforward fashion.

4. Wess-Zumino-Witten quantum field theory

As a minimal SU(n) model, we discuss the realization of a strongly conformal field theory with an integrable 1D SU(3) Heisenberg model. Here we investigate the universal features of the SU(3)$_1$ Wess-Zumino-Witten (WZW) quantum field theory of level $k = 1$. In particular, we extract the conformal data by accessing the entanglement entropy for a 1D SU(3) Heisenberg model at the Ulmin-Lai-Sutherland (ULS) critical point, the parent Hamiltonian for generating a collection of strongly correlated ground states, such as those found in fractional quantum Hall systems. Because of the versatile programmability, the gauged waveguide QED simulator can be readily extended to the low-energy states of the 2D antiferromagnetic SU(n) model (10), which are described by

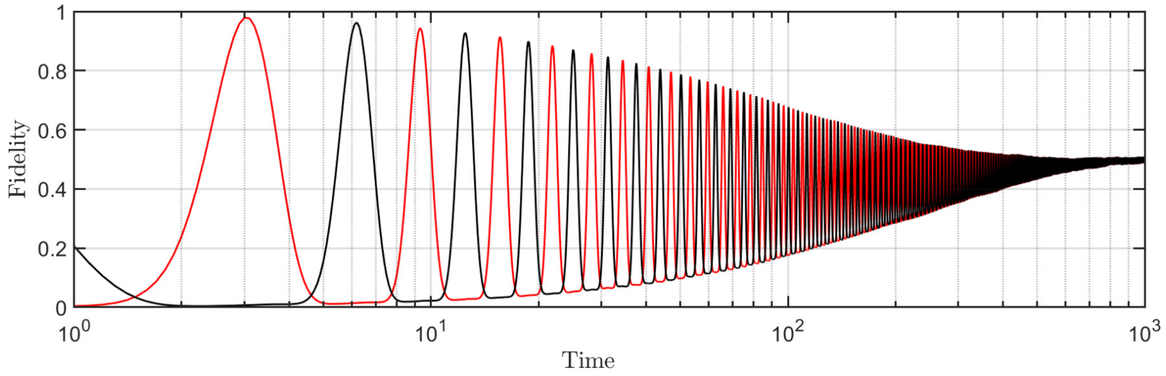

FIG. 10. Quantum-state transfer over a dissipative spin chain. The open-system dynamics is numerically computed for the quantum-state transfer across $N = 6$ atoms with the figure of merit $\mathcal{F} \simeq 10^4$ by the quantum trajectory method. In addition to the intrinsic mechanical dissipation, we include spin-relaxation processes in the far-off-resonance optical trap. The state fidelity of the first (last) atom in the spin chain is displayed as a black (red) line.

the (2+1)D WZW conformal field theory and holographically connected to a 3D Chern-Simons quantum gravity in the scaling limit.

Specifically, we consider the realization of a (1+1)D $\mathrm{SU}(3)_1$ WZW CFT for the antiferromagnetic SU(3) Heisenberg model

$$\hat{H}_{\mathrm{WZW}} = \mathcal{J}_c \sum_{\bar{i}} \sum_{\alpha} \hat{\Lambda}_{\alpha}^{(\bar{i})} \hat{\Lambda}_{\alpha}^{(\bar{i}+1)} \tag{C6}$$

for the logical SU(3) spins on a ring within the sector of $\mathcal{Q} = n - 2$ of the waveguide QED simulator. Since $\mathcal{J}_{\bar{i},\bar{j}} = -O_{\bar{i},\bar{j}}^2/2\Lambda_G < 0$, the vacuum state of the WZW CFT is encoded onto the most excited state of Eq. (C6) within the sector $\mathcal{Q}$. This model has been extensively studied in the context of Haldane phase of the bilinear biquadratic (BBQ) spin-1 model

$$\hat{H}_{\mathrm{BBQ}} = \mathcal{J}_c \sum_{\bar{i}} \cos\theta \hat{\mathbf{S}}_{\bar{i}} \hat{\mathbf{S}}_{\bar{i}+1} + \sin\theta (\hat{\mathbf{S}}_{\bar{i}} \hat{\mathbf{S}}_{\bar{i}+1})^2. \tag{C7}$$

The enlarged SU(3) symmetry of Eq. (C6) [Eq. (C7) at $\theta_{\mathrm{ULS}} = \pi/4$] can be thought of as the consequence of the critical point of Berezinskii-Kosterlitz-Thouless (BKT) transition between the massive Haldane phase and an extended critical phase, described by the WZW field theory.

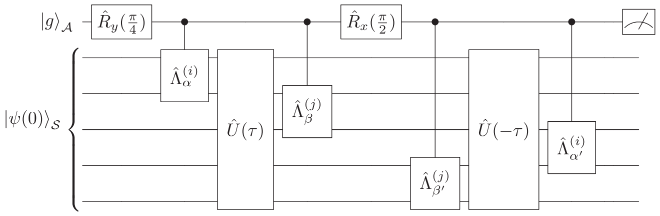

FIG. 11. Construction of SU(n) OTOCs $C_{\alpha,\beta,\alpha',\beta'}$ and measurement prescription of highly complex OTOCs. The circuit constructs the OTOC variables $C_{\alpha,\beta,\alpha',\beta'} \equiv \langle \hat{\Lambda}_{\beta'}^{(j)}(t) \hat{\Lambda}_{\alpha'}^{(i)}(0) \hat{\Lambda}_{\beta}^{(j)}(t) \hat{\Lambda}_{\alpha}^{(i)}(0) \rangle$ of system atoms $\mathcal{S}$ and maps the values to the internal state of a single ancilla qubit $\mathcal{A}$. The time-inverse evolution for the global dynamics $\hat{U}(-\tau) = e^{-i(-\hat{H}_{\mathrm{SY}})\tau}$ can be realized still in a positive time flow but with a negative Hamiltonian $-\hat{H}_{\mathrm{SY}}$, i.e., inverting the sign of all $\mathcal{J}_{ij}$.

a. Enlarged SU(3) symmetry of bilinear biquadratic spin-1 models

To understand the relationship between the familiar Haldane gap for spin-1 Heisenberg magnets at the exactly solvable point $\theta_{\mathrm{AKLT}} = \arctan(\frac{1}{3})$ (AKLT valence bond state) and the massless WZW field theory at $\theta_{\mathrm{ULS}} = \pi/4$ [see also Fig. 4(b)], we describe how the SU(3)-breaking marginal operator in the vicinity to the SU(3)-symmetric critical point θ_{ULS} deforms the WZW CFT and dynamically generate a mass term in the Haldane phase by way of a BKT transition [68]. By moving into the fermionic parton picture defined in Sec. V, the BBQ Hamiltonian can be mapped to

$$\hat{\mathcal{H}}_{\mathrm{parton}}^{\mathrm{BBQ}} = \hat{\mathcal{H}}_{\mathrm{parton}} + \epsilon^2 \hat{\mathcal{H}}_{\mathrm{marginal}}, \tag{C8}$$

under the constraint $\sum_{\alpha} \hat{\psi}_{\alpha}^{(\bar{i})\dagger} \hat{\psi}_{\alpha}^{(\bar{i})} = 1$. The SU(3)-symmetric parton Hamiltonian $\hat{\mathcal{H}}_{\mathrm{parton}}$, defined in Eq. (11), is the dominant term near the ULS point and kinetically exchanges excitations between the sites. The marginal operator $\hat{\mathcal{H}}_{\mathrm{marginal}} = \mathcal{J} \sum_{\bar{i}} \hat{\psi}_{\alpha}^{(\bar{i})\dagger} \hat{\psi}_{\beta}^{(\bar{i})} \hat{\psi}_{\alpha}^{(\bar{i}+1)\dagger} \hat{\psi}_{\beta}^{(\bar{i}+1)}$, proportional to $\epsilon^2 = \tan\theta - 1$, projects the neighboring sites to the singlet space, similar to the singlet projectors of the AKLT Hamiltonian.

By applying the Hubbard-Stratonovich transformation to Eq. (C8) at the ULS point θ_{ULS}, we obtain the mean-field Hamiltonian $\hat{H}_{\mathrm{mf}} = |\chi_{\bar{i},\bar{i}+1}|^2 + \mu_{\bar{i}}(\hat{\psi}_{\alpha}^{(\bar{i})} \hat{\psi}_{\alpha}^{(\bar{i})} - 1) - \chi_{\bar{i},\bar{i}+1} \hat{\psi}_{\alpha}^{(\bar{i})\dagger} \hat{\psi}_{\alpha}^{(\bar{i}+1)} + \mathrm{H.c.}$ with the auxiliary fields $\chi_{\bar{i},\bar{i}+1} = \langle \hat{\psi}_{\beta}^{(\bar{i})\dagger} \hat{\psi}_{\beta}^{(\bar{i}+1)} \rangle$ and the constraints expressed in terms of the chemical potential $\mu_{\bar{i}}$, with a Fermi sea filled up to the momentum $k_F = \pi/3$. Around this saddle point, the low-energy physics of Eq. (C8) at θ_{ULS} is described by $\hat{\psi}_{\alpha}^{(\bar{i})\dagger} = e^{ik_F x_{\bar{i}}} \hat{\psi}_{L,\alpha}(x_{\bar{i}}) + e^{-ik_F x_{\bar{i}}} \hat{\psi}_{R,\alpha}(x_{\bar{i}})$ with the chiral fermions $\hat{\psi}_{L,\alpha}(x)$, $\hat{\psi}_{R,\alpha}(x)$ only populated at the Fermi points and we write Eq. (C8) as

$$\hat{\mathcal{H}}(x) \simeq \pi v_F \int dx \sum_{\alpha,\beta} \left(\hat{j}_R^{\alpha,\beta} \hat{j}_R^{\beta,\alpha} + \hat{j}_L^{\alpha,\beta} \hat{j}_L^{\beta,\alpha} \right)$$

$$+\epsilon^2 \left(\hat{j}_R^{\alpha,\beta} \hat{j}_R^{\alpha,\beta} + \hat{j}_L^{\alpha,\beta} \hat{j}_L^{\alpha,\beta} \right) \tag{C9}$$

in terms of U(3) currents $\hat{j}_L^{\alpha,\beta} (\hat{j}_R^{\alpha,\beta}) = \hat{\psi}_{L,\alpha}^{\dagger} \hat{\psi}_{L,\beta} (\hat{\psi}_{R,\alpha}^{\dagger} \hat{\psi}_{R,\beta})$ and Fermi velocity v_F.

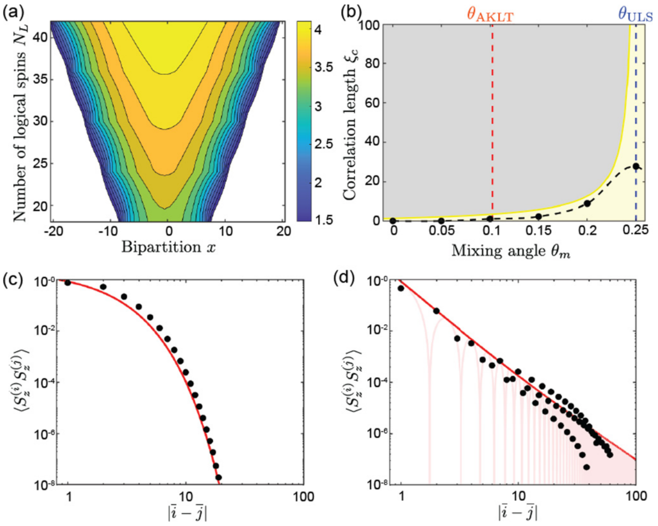

FIG. 12. Bilinear biquadratic spin-1 model. (a) CFT scaling of entanglement entropy at the ULS point $\theta_{\mathrm{ULS}} = \pi/4$. (b) Quantum phase transition between the gapped Haldane phase and gapless nematic phase at the ULS quantum critical point. (c) Spin-spin correlation function $\langle \hat{S}_z^{(\bar{i})} \hat{S}_z^{(\bar{j})} \rangle$ at the Affleck-Lieb-Kennedy-Tasaki (AKLT) point $\theta_{\mathrm{AKLT}} = \arctan(\frac{1}{3})$ with a valence-bond ground state. (d) Spin-spin correlation function $\langle \hat{S}_z^{(\bar{i})} \hat{S}_z^{(\bar{j})} \rangle$ at the ULS point $\theta_{\mathrm{ULS}} = \pi/4$. The correlation functions and the phase diagram are computed from the uniform MPSs, optimized by the infinite DMRG algorithm with truncated bond dimension up to $\chi = 500$. Finite χ generates an artificial cutoff in the correlation length ξ_c to the otherwise algebraic correlation function. The fitting thereby only takes $|\bar{i} - \bar{j}| < \xi_c \simeq 40$ as the input. The entanglement entropy is simulated from a finite MPS for the logical SU(3) spins (three physical spins per logical spin) on a ring with bond dimension up to $\chi = 8000$.

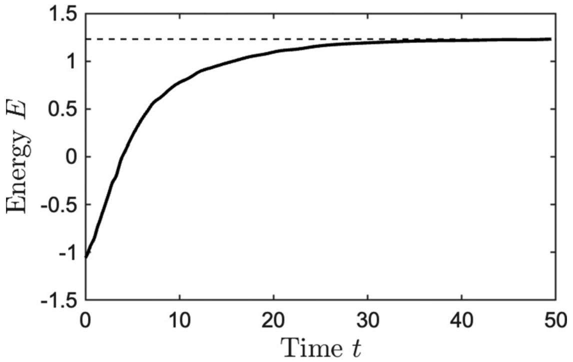

FIG. 13. Complex-time matrix-product state evolution. The random MPS is initially prepared for 54 physical spins ($N_L = 18$ logical spins) and the MPS is evolved under complex-time coordinates [Eq. (C11)] by way of the TEBD algorithm with an open boundary condition. At each time step, the SU(2) MPS of the physical spins is transformed to the SU(3) MPS for the logical spins by locally contracting the SU(2) MPS with an isometric matrix-product operator that projects the physical spins to the low-energy sector $\mathcal{Q}$. The overall dynamics is described by a cooling (heating) to (within) the ground-state sector $\mathcal{Q}$, corresponding to the preparation of the vacuum state of the WZW CFT. The dashed line indicates the DMRG ground-state energy obtained for the target WZW Hamiltonian. The maximum bond dimension is $\chi = 200$.

For the first term [with a global $\mathrm{U}(3) = \mathrm{U}(1) \oplus \mathrm{SU}(3)$ symmetry], a U(1) charge gap opens and leaves the SU(3)-symmetric WZW model $\hat{\mathcal{H}}_{\mathrm{WZW}}$ at the low-energy sector. Following the Abelian bosonization procedure $\hat{\psi}_{L,\alpha} = :1/2\pi \exp(-i\sqrt{4\pi}\hat{\phi}_\alpha)$: of Ref. [68], the SU(3)-symmetric continuum Hamiltonian reads

$$\hat{\mathcal{H}}_{\mathrm{WZW}} \sim \int dx(\partial\phi_1\partial\phi_1 + \partial\phi_2\partial\phi_2 + \mathbb{A}), \tag{C10}$$

where $\mathbb{A}$ denotes the antiholomorphic part, with two compact SU(3) boson fields $\phi_{1,2}$ (each with central charge $c = 1$). Figure 12(a) depicts the CFT scaling behavior of entanglement entropy following the Calabrese-Cardy formula for different system size N_L ($c = 2.05 \pm 0.03$). The entanglement entropy is computed by system-size expansion of finite matrix-product states for logical spins on a ring with a maximum bond dimension $\chi = 8000$. The finite MPS was optimized using a hybrid complex-time evolution algorithm (Sec. VI). Following the operator product expansion, it can be shown that $\langle \hat{S}_z^{(\bar{i})} \hat{S}_z^{(\bar{j})} \rangle_{\mathrm{ULS}} \sim \frac{\cos(2k_F|\bar{i}-\bar{j}|)}{|\bar{i}-\bar{j}|^{2\mathcal{D}}}$ with a scaling dimension $\mathcal{D} = 2/3$ [105]. Figure 12(d) displays the correlation function obtained by optimizing uniform MPSs with an infinite DMRG algorithm truncated to $\chi = 500$ and the scaling dimension is fitted to $\mathcal{D} = 0.68 \pm 0.03$. The marginal perturbation of Eq. (C9), on the other hand, breaks the global SU(3) symmetry of the ULS point, and a mass gap $m_\theta = \exp[-\gamma(\theta_{\mathrm{ULS}} - \theta)^{-0.6}]$ is dynamically generated for increasing coupling constant $\epsilon > 0$ ($\theta < \theta_{\mathrm{ULS}}$) with spin-spin correlation $\langle \hat{S}_z^{(\bar{i})} \hat{S}_z^{(\bar{j})} \rangle_\theta \sim \cos(2k_F|\bar{i} - \bar{j}|)e^{-m_\theta|\bar{i}-\bar{j}|}$ and nonuniversal constant γ. The asymptotic freedom of the marginal interaction at $\epsilon > 0$ can be thought of as a BKT phase transition in terms of the renormalization group flow [105]. The yellow line of Fig. 12(b) illustrates the scaling behavior of the correlation length $\eta_c \sim 1/m_\theta$ in comparison to those obtained from uniform MPSs, where the nonuniversal constant γ is fitted to the data points. The maximum correlation length $\xi_c \simeq 40$ at the ULS point is artificially cut off due to the finite $\chi = 500$ truncation to the uniform MPS.

b. Hybrid complex-time algorithm

Because the vacuum state of WZW CFT corresponds to the most excited state within the low-energy sector $\mathcal{Q}$, standard DMRG algorithms cannot be adequately adapted to access the ground state of the target Hamiltonians [see also the inset of Fig. 4(a)]. We instead apply a hybrid complex-time evolution to a random MPS in order to relax the system to the most excited state (target ground state) within the ground-state sector of the simulator by way of a time-evolving block decimation algorithm on the modified Hamiltonian

$$\hat{H} = \sum_{\bar{i},\bar{j}} (\hat{O}_{\bar{i},\bar{j}} + \hat{D}_{\bar{i},\bar{j}}) + i\hat{H}_G, \tag{C11}$$

with the definitions of $\hat{O}_{\bar{i},\bar{j}}$, $\hat{D}_{\bar{i},\bar{j}}$, $\hat{H}_G$ in Sec. IV. The imaginary constraint $\hat{H}_G$ allows the cooling of the random MPS to the sector $\mathcal{Q}$, while the first term mediates the gauge-invariant ring-exchange Hamiltonian (C4) with an imaginary $\mathcal{J}_{\bar{i},\bar{j}} = iO_{\bar{i},\bar{j}}^2/2\Lambda_G$, which heats the system to the most excited state of the low-energy sector $\mathcal{Q}$.

Following the complex-time evolution, an isometric matrix-product projector (MPO) is locally contracted with the time-evolved MPS to map the physical SU(2) spins to the logical SU(3) spins. While the isometric tensor is not necessary to the protocol, we have found that such a practice allows a more intuitive interpretation on the operations taking place in the logical degrees of freedom. In particular, the converted MPS obtained through this method coincides with that obtained by performing a finite DMRG on the logical WZW Hamiltonian in Eq. (C6). Figure 13 displays the energy relaxation for the hybrid algorithm (solid line), which prepares the vacuum state of the WZW CFT (dashed line).

[1] S. Lloyd, Universal quantum simulators, Science **273**, 1073 (1996).

[2] L. Amico, R. Fazio, A. Osterloh, and V. Vedral, Entanglement in many-body systems, Rev. Mod. Phys. **80**, 517 (2008).

[3] H. J. Kimble, The quantum internet, Nature (London) **453**, 1023 (2008).

[4] I. Bloch, J. Dalibard, and W. Zwerger, Many-body physics with ultracold gases, Rev. Mod. Phys. **80**, 885 (2008).

[5] T. S. Cubitt, A. Montanaro, and S. Piddock, Universal quantum Hamiltonians, Proc. Natl. Acad. Sci. U.S.A. **115**, 9497 (2018).

[6] J. D. Biamonte and P. J. Love, Realizable Hamiltonians for universal adiabatic quantum computers, Phys. Rev. A **78**, 012352 (2008).

[7] D. Nagaj and P. Wocjan, Hamiltonian quantum cellular automata in one dimension, Phys. Rev. A **78**, 032311 (2008).

[8] K. G. H. Vollbrecht and J. I. Cirac, Quantum Simulators, Continuous-Time Automata, and Translationally Invariant Systems, Phys. Rev. Lett. **100**, 010501 (2008).

[9] S. John and J. Wang, Quantum Electrodynamics Near a Photonic Band Gap: Photon Bound States and Dressed Atoms, Phys. Rev. Lett. **64**, 2418 (1990).

[10] G. Kurizki, Two-atom resonant radiative coupling in photonic band structures, Phys. Rev. A **42**, 2915 (1990).

[11] S. John and T. Quang, Quantum Optical Spin-Glass State of Impurity Two-Level Atoms in a Photonic Band Gap, Phys. Rev. Lett. **76**, 1320 (1996).

[12] C.-L. Hung, S. M. Meenehan, D. E. Chang, O. Painter, and H. J. Kimble, Trapped atoms in one-dimensional photonic crystals, New J. Phys. **15**, 083026 (2013).

[13] J. D. Thompson, T. G. Tiecke, N. P. de Leon, J. Feist, A. V. Akimov, M. Gullans, A. S. Zibrov, V. Vuletić, and M. D. Lukin, Coupling a single trapped atom to a nanoscale optical cavity, Science **340**, 1202 (2013).

[14] T. G. Tiecke, J. D. Thompson, N. P. de Leon, L. R. Liu, V. Vuletić, and M. D. Lukin, Nanophotonic quantum phase switch with a single atom, Nature (London) **508**, 241 (2014).

[15] A. Goban, C.-L. Hung, S.-P. Yu, J. D. Hood, J. A. Muniz, J. H. Lee, M. J. Martin, A. C. McClung, K. S. Choi, D. E. Chang, O. Painter, and H. J. Kimble, Atom-light interactions in photonic crystals, Nat. Commun. **5**, 3808 (2014).

[16] A. Goban, C.-L. Hung, J. D. Hood, S.-P. Yu, J. A. Muniz, O. Painter, and H. J. Kimble, Superradiance for Atoms Trapped Along a Photonic Crystal Waveguide, Phys. Rev. Lett. **115**, 063601 (2015).

[17] J. D. Hood, A. Goban, A. Asenjo-Garcia, M. Lu, S.-P. Yu, D. E. Chang, and H. J. Kimble, Atom-atom interactions around the band edge of a photonic crystal waveguide, Proc. Natl. Acad. Sci. U.S.A. **113**, 10507 (2016).

[18] P. Samutpraphoot, T. Đorđević, P. L. Ocola, H. Bernien, C. Senko, V. Vuletić, and M. D. Lukin, Strong Coupling of Two Individually Controlled Atoms via a Nanophotonic Cavity, Phys. Rev. Lett. **124**, 063602 (2020).

[19] T. Dordević, P. Samutpraphoot, P. L. Ocola, H. Bernien, B. Grinkemeyer, I. Dimitrova, V. Vuletić, and M. D. Lukin, Nanophotonic quantum interface and transportable entanglement for atom arrays, Science **373**, 1511 (2021).

[20] J. S. Douglas, H. Habibian, C.-L. Hung, A. V. Gorshkov, H. J. Kimble, and D. E. Chang, Quantum many-body models with cold atoms coupled to photonic crystals, Nat. Photon. **9**, 326 (2015).

[21] T. Shi, Y.-H. Wu, A. Gonzalez-Tudela, and J. I. Cirac, Bound States in Boson Impurity Models, Phys. Rev. X **6**, 021027 (2016).

[22] G. Calajo, F. Ciccarello, D. E. Chang, and P. Rabl, Atom-field dressed states in slow-light waveguide QED, Phys. Rev. A **93**, 033833 (2016).

[23] M. Gullans, T. G. Tiecke, D. E. Chang, J. Feist, J. D. Thompson, J. I. Cirac, P. Zoller, and M. D. Lukin, Nanoplasmonic Lattices for Ultracold Atoms, Phys. Rev. Lett. **109**, 235309 (2012).

[24] A. Gonzalez-Tudela, C.-L. Hung, D. E. Chang, J. I. Cirac, and H. J. Kimble, Subwavelength vacuum lattices and atom-atom interactions in two-dimensional photonic crystals, Nat. Photon. **9**, 320 (2015).

[25] C.-L. Hung, A. Gonzelez-Tudela, J. I. Cirac, and H. J. Kimble, Quantum spin dynamics with pairwise-tunable, long-range interactions, Proc. Natl. Acad. Sci. U.S.A. **113**, E4946 (2016).

[26] M. J. Harmann, F. G. S. L. Brandao, and M. B. Plenio, Strongly interacting polaritons in coupled arrays of cavities, Nat. Phys. **2**, 849 (2006).

[27] A. D. Greentree, C. Tahan, J. H. Cole, and L. C. L. Hollenberg, Quantum phase transitions of light, Nat. Phys. **2**, 856 (2006).

[28] T. Ramos, H. Pichler, A. J. Daley, and P. Zoller, Quantum Spin Dimers from Chiral Dissipation in Cold-Atom Chains, Phys. Rev. Lett. **113**, 237203 (2014).

[29] P. Lodahl, S. Mahmoodian, S. Stobbe, A. Rauschenbeutel, P. Schneeweiss, J. Volz, H. Pichler, and P. Zoller, Chiral quantum optics, Nature (London) **541**, 473 (2017).

[30] H. Pichler, S. Choi, P. Zoller, and M. D. Lukin, Universal photonic quantum computation via time-delayed feedback, Proc. Natl. Acad. Sci. U.S.A. **114**, 11362 (2017).

[31] M. T. Manzoni, L. Mathey, and D. E. Chang, Designing exotic many-body states of atomic spin and motion in photonic crystals, Nat. Commun. **8**, 14696 (2017).

[32] L. Balents, Spin liquids in frustrated magnets, Nature (London) **464**, 199 (2010).

[33] S. Sachdev, Bekenstein-Hawking Entropy and Strange Metals, Phys. Rev. X **5**, 041025 (2015).

[34] A. Y. Kitaev, A simple model of quantum holography, Talks at KITP Program: Entanglement in Strongly-Correlated Quantum Matter, 2015 (unpublished), available at https://online.kitp.ucsb.edu/online/entangled15/.

[35] E. Witten, Non-Abelian bosonization in two dimensions, Commun. Math. Phys. **92**, 455 (1984).

[36] S. John, Strong Localization of Photons in Certain Disordered Dielectric Superlattices, Phys. Rev. Lett. **58**, 2486 (1987).

[37] T. Gruner and D.-G. Welsch, Green-function approach to the radiation-field quantization for homogeneous and inhomogeneous Kramers-Kronig dielectrics, Phys. Rev. A **53**, 1818 (1996).

[38] H. T. Dung, L. Knöll and D.-G. Welsch, Resonat dipole-dipole interaction in the presence of dispersing and absorbing surroundings, Phys. Rev. A **66**, 063810 (2002).

[39] G. Angelatos, Theory and applications of light-matter interactions in quantum dot nanowire photonic crystal systems, Ph.D. thesis, Queens University, 2015.

[40] A. Asenjo-Garcia, J. D. Hood, D. E. Chang, and H. J. Kimble, Atom-light interactions in quasi-one-dimensional nanostructures: A Green's-function perspective, Phys. Rev. A **95**, 033818 (2017).

[41] A. Asenjo-Garcia, M. Moreno-Cardoner, A. Albrecht, H. J. Kimble, and D. E. Chang, Exponential Improvement in Photon Storage Fidelities Using Subradiance and Selective Radiance in Atomic Arrays, Phys. Rev. X **7**, 031024 (2017).

[42] D. Jaksch and P. Zoller, Creation of effective magnetic fields in optical lattices: The Hofstadter butterfly for cold neutral atoms, New J. Phys. **5**, 56 (2003).

[43] A. Bermudez, T. Schaetz, and D. Porras, Synthetic Gauge Fields for Vibrational Excitations of Trapped Ions, Phys. Rev. Lett. **107**, 150501 (2011).

[44] S. Korenblit, D. Kafri, W. C. Campbell, R. Islam, E. E. Edwards, Z.-X. Gong, G.-D. Lin, L.-M. Duan, J. Kim, K. Kim, and C. Monroe, Quantum simulation of spin models on an arbitrary lattice with trapped ions, New J. Phys. **14**, 095024 (2012).

[45] M. Aidelsburger, M. Atala, M. Lohse, J. T. Barreiro, B. Paredes, and I. Bloch, Realization of the Hofstadter Hamiltonian with Ultracold Atoms in Optical Lattices, Phys. Rev. Lett. **111**, 185301 (2013).

[46] F. Reiter and A. S. Sørensen, Effective operator formalism for open quantum systems, Phys. Rev. A **85**, 032111 (2012).

[47] V. Kalmeyer and R. B. Laughlin, Equivalence of the Resonating-Valence-Bond and Fractional Quantum Hall States, Phys. Rev. Lett. **59**, 2095 (1987).

[48] B. Bauer, L. Cincio, B. P. Keller, M. Dolfi, G. Vidal, S. Trebst, and A. W. W. Ludwig, Chiral spin liquid and emergent anyons in a kagome lattice Mott insulator, Nat. Commun. **5**, 5137 (2014).

[49] K. Kumar, K. Sun, and E. Fradkin, Chiral spin liquids on the kagome lattice, Phys. Rev. B **92**, 094433 (2015).

[50] K. Essafi, O. Benton, and L. D. C. Jaubert, A kagome map of spin liquids from XXZ to Dzyaloshinskii-Moriya ferromagnet, Nat. Commun. **7**, 10297 (2015).

[51] L. Balents, M. P. A. Fisher, and S. M. Girvin, Fractionalization in an easy-axis kagome antiferromagnet, Phys. Rev. B **65**, 224412 (2002).

[52] S. V. Isakov, M. B. Hastings, and R. G. Melko, Topological entanglement entropy of a Bose-Hubbard spin liquid, Nat. Phys. **7**, 772 (2011).

[53] M. J. P. Gingras and P. A. McClarty, Quantum spin ice: A search for gapless quantum spin liquids in pyrochlore magnets, Rep. Prog. Phys. **77**, 056501 (2014).

[54] C. Castelnovo, R. Moessner, and S. L. Sondhi, Magnetic monopoles in spin ice, Nature (London) **451**, 42 (2008).

[55] A. V. Gorshkov, M. Hermele, V. Gurarie, C. Xu, P. S. Julienne, J. Ye, P. Zoller, E. Demler, M. D. Lukin, and A. M. Rey, Two-orbital $SU(N)$ magnetism with ultracold alkaline-earth atoms, Nat. Phys. **6**, 289 (2010).

[56] Y. Tokura and N. Nagaosa, Orbital physics in transition-metal oxides, Science **288**, 462 (2000).

[57] N. Read and S. Sachdev, Valence-bond and Spin-Peierls Ground States of Low-Dimensional Quantum Antiferromagnets, Phys. Rev. Lett. **62**, 1694 (1989).

[58] J. B. Marston and I. Affleck, Large-n limit of the Hubbard-Heisenberg model, Phys. Rev. B **39**, 11538 (1989).

[59] M. Greiter and S. Rachel, Valence bond solids for SU(n) spin chains: Exact models, spinon confinement, and the Haldane gap, Phys. Rev. B **75**, 184441 (2007).

[60] I. Affleck, Quantum spin chains and the Haldane gap, J. Phys.: Condens. Matter **1**, 3047 (1989).

[61] J. Wess and B. Zumino, Consequences of anomalous ward identities, Phys. Lett. B **37**, 95 (1971).

[62] S. Sachdev and J. Ye, Gapless Spin-Fluid Ground State in a Random Quantum Heisenberg Magnet, Phys. Rev. Lett. **70**, 3339 (1993).

[63] A. Kitaev, Hidden correlations in the Hawking radiation and thermal noise, Talks at the Fundamental Physics Prize Symposium, 2014 (unpublished), available at https://online.kitp.ucsb.edu/online/joint98/kitaev/.

[64] S. H. Shenker and D. Stanford, Black holes and the butterfly effect, J. High Energy Phys. 03 (2014) 067.

[65] J. Maldacena, S. H. Shenker, and D. Stanford, A bound on chaos, J. High Energy Phys. **8** (2014)106 .

[66] E. Witten, Global aspects of current algebra, Nucl. Phys. B **223**, 422 (1983).

[67] E. Witten, Quantum field theory and the Jones polynomial, Commun. Phys. **121**, 351 (1989).

[68] O. M. Sule, H. J. Changlani, I. Maruyama, and S. Ryu, Determination of Tomonaga-Luttinger parameters for a two-component liquid, Phys. Rev. B **92**, 075128 (2015).

[69] M. Dalmonte, B. Vermersh, and P. Zoller, Quantum simulation and spectroscopy of entanglement Hamiltonians, Nat. Phys. **14**, 827 (2018).

[70] H. Li and F. D. M. Haldane, Entanglement Spectrum as a Generalization of Entanglement Entropy: Identification of Topological Order in Non-Abelian Fraction Quantum Hall Effect States, Phys. Rev. Lett. **101**, 010504 (2008).

[71] C. Senko, J. Smith, P. Richerme, A. Lee, W. C. Campbell, and C. Monroe, Coherent imaging spectroscopy of a quantum many-body spin system, Science **345**, 430 (2014).

[72] C. Holzhey, F. Larsen, and F. Wilczek, Geometric and renormalized entropy in conformal field theory, Nucl. Phys. B **424**, 443 (1994).

[73] P. Calabrese and J. Cardy, Entanglement entropy and conformal field theory, J. Phys. A: Math. Theor. **42**, 504005 (2009).

[74] D. Barredo, S. de Leseleuc, V. Lienhard, T. Lahaye, and A. Browaeys, An atom-by-atom assembler of defect-free arbitrary 2D atomic arrays, Science **354**, 1021 (2016).

[75] M. Endres, H. Bernien, A. Keesling, H. Levine, E. R. Anschuetz, A. Krajenbrink, C. Senko, V. Vuletic, M. Greiner, and M. D. Lukin, Atom-by-atom assembly of defect-free one-dimensional cold atom arrays, Science **354**, 1024 (2016).

[76] H. Kim, W. Lee, H.-G. Lee, H. Jo, Y. Song, and J. Ahn, *In situ* single-atom array synthesis using dynamic holographic optical tweezers, Nat. Commun. **7**, 13317 (2016).

[77] Y. Meng, A. Dareau, P. Schneeweiss, and A. Rauschenbeutel, Near-Ground-State Cooling of Atoms Optically Trapped 300 nm Away from a Hot Surface, Phys. Rev. X **8**, 031054 (2018).

[78] P. L. McMahon, A. Marandi, Y. Haribara, R. Hamerly, C. Langrock, S. Tamate, T. Inagaki, H. Takesue, S. Utsunomiya, K. Aihara, R. L. Byer, M. M. Fejer, H. Mabuchi, and Y. Yamamoto, A fully-programmable 100-spin coherent Ising machine with all-to-all connections, Science **354**, 614 (2016).

[79] Y. Haribara, H. Ishikawa, S. Utsunomiya, K. Aihara, and Y. Yamamoto, Performance evaluation of coherent Ising machines against classical neural networks, Quantum Sci. Technol. **2**, 044002 (2017).

[80] X. Luan, J.-B. Béguin, A. P. Burgers, Z. Qin, S.-P. Yu, and H. J. Kimble, The integration of photonic crystal waveguides with atom arrays in optical tweezers, Adv. Quantum Technol. **3**, 2000008 (2020).

[81] A. Kitaev, Fault-tolerant quantum computation by anyons, Ann. Phys. (NY) **303**, 2 (2003).

[82] S. Bose, Quantum Communication Through an Unmodulated Spin Chain, Phys. Rev. Lett. **91**, 207901 (2003).

[83] M. Christandl, N. Datta, A. Ekert, and A. J. Landahl, Perfect State Transfer in Quantum Spin Networks, Phys. Rev. Lett. **92**, 187902 (2004).

[84] M. Paternostro, G. M. Palma, M. S. Kim, and C. Falci, Quantum-state transfer in imperfect artificial spin networks, Phys. Rev. A **71**, 042311 (2005).

[85] M.-H. Yung and S. Bose, Perfect state transfer, effective gates, and entanglement generation in engineered bosonic and fermionic networks, Phys. Rev. A **71**, 032310 (2005).

[86] C. Di Franco, M. Paternostro, and M. S. Kim, Perfect State Transfer on a Spin Chain without State Initialization, Phys. Rev. Lett. **101**, 230502 (2008).

[87] N. Y. Yao, L. Jiang, A. V. Gorshkov, P. C. Maurer, G. Giedke, J. I. Cirac, and M. D. Lukin, Scalable architecture for a room temperature solid-state quantum information processor, Nat. Commun. **3**, 800 (2011).

[88] N. Y. Yao, C. R. Laumann, A. V. Gorshkov, H. Weimer, L. Jiang, J. I. Cirac, P. Zoller, and M. D. Lukin, Topologically protected quantum state transfer in a chiral spin liquid, Nat. Commun. **4**, 1585 (2013).

[89] M. Levin and X. Wen, String-net condensation: A physical mechanism for topological phases, Phys. Rev. B **71**, 045110 (2005).

[90] P. M. Poggi and D. A. Wisniacki, Optimal control of many-body quantum dynamics: Chaos and complexity, Phys. Rev. A **94**, 033406 (2016).

[91] S.-P. Yu, J. D. Hood, J. A. Muniz, M. J. Martin, R. Norte, C.-L. Hung, S. M. Meenehan, J. D. Cohen, O. Painter, and H. J. Kimble, Nanowire photonic crystal waveguides for single atom trapping and strong light-matter interactions, Appl. Phys. Lett. **104**, 111103 (2014).

[92] T. F. Krauss, Slow-light in photonic crystal waveguides, J. Phys. D **40**, 2666 (2007).

[93] M. Arcari, I. Söllner, A. Javadi, S. Lindskov Hansen, S. Mahmoodian, J. Liu, H. Thyrrestrup, E. H. Lee, J. D. Song, S. Stobbe, and P. Lodahl, Near-Unity Coupling Efficiency of a Quantum Emitter to a Photonic Crystal Waveguide, Phys. Rev. Lett. **113**, 093603 (2014).

[94] P. Lodahl, S. Mahmoodian, and S. Stobbe, Interfacing single photons and single quantum dots with photonic nanostructures, Rev. Mod. Phys. **87**, 347 (2015).

[95] S. G. Johnson and J. D. Joannopoulos, Block-iterative frequency-domain methods for Maxwell's equations in a plane-wave basis, Opt. Express **8**, 173 (2001).

[96] A. F. Oskooi, D. Roundy, M. Ibanescu, P. Bermel, J. D. Joannopoulos, and S. G. Johnson, MEEP: A flexible free-software package for electromagnetic simulations by the FDTD method, Comput. Phys. Commun. **181**, 687 (2010).

[97] W. Shin and S. Fan, Choice of the perfectly matched layer boundary condition for frequency-domain Maxwell's equations solvers, J. Comput. Phys. **231**, 3406 (2012).

[98] K. Sakoda, *Optical Properties of Photonic Crystals*, Springer Series in Optical Sciences Vol. 80 (Springer, Berlin, 2005).

[99] C. P. Van Vlack and S. Hughes, Finite-difference time-domain technique as an efficient tool for calculating the regularized Green function: Applications to the local-field problem in quantum optics for inhomogeneous lossy materials, Opt. Lett. **37**, 2880 (2012).

[100] M. Kanskar, P. Paddon, V. Pacradouni, R. Morin, A. Busch, J. F. Young, S. R. Johnson, J. MacKenzie, and T. Tiedje, Observation of leaky slab modes in an air-bridged semiconductor waveguide with a two-dimensional photonic lattice, Appl. Phys. Lett. **70**, 1438 (1997).

[101] K. B. Crozier, V. Lousse, O. Kilic, S. Kim, S. Fan, and O. Solgaard, Air-bridged photonic crystal slabs at visible and near-infrared wavelengths, Phys. Rev. B **73**, 115126 (2006).

[102] S. Bernard, C. Reinhardt, V. Dumont, Y.-A. Peter, and J. C. Sankey, Precision resonance tuning and design of SiN photonic crystal reflectors, Opt. Lett. **41**, 5624 (2016).

[103] F. Gerbier and Y. Castin, Heating rates for an atom in a far-detuned optical lattice, Phys. Rev. A **82**, 013615 (2010).

[104] R. A. Cline, J. D. Miller, M. R. Matthews, and D. J. Heinzen, Spin relaxation of optically trapped atoms by light scattering, Opt. Lett. **19**, 207 (1994).

[105] C. Itoi and M.-H. Kato, Extended massless phase and the Haldane phase in a spin-1 isotropic antiferromagnetic chain, Phys. Rev. B **55**, 8295 (1997).